










Research article

Enhanced photocatalysis of natural rubber foams filters boosted by modified-titanium oxide hybrid fillers: Gaseous benzene removal, antibacterial properties and air permeability

Pornsiri Toh-ae¹, Prachid Saramolee², Siriluk Chiarakorn³, Dujduan Waraho-Zhmayev⁴, Attapol Kamthong⁴, Raymond Lee Nip⁵, Ekwipoo Kalkornsuraanee⁶, Jobish Johns⁷, Patcharapit Promoppatum⁸, Yeampon Nakaramontri^{1*}

¹Sustainable Polymer & Innovative Composites Material Research Group, Department of Chemistry, Faculty of Science, King Mongkut's University of Technology Thonburi, Bangkok, Thailand

²Petrochemical and Polymer, School of Engineering and Technology, Walailak University, Nakhonsithammarat, Thailand

³Environmental Technology Program, School of Energy, Environment and Materials, King Mongkut's University of Technology Thonburi, Bangkok, Thailand

⁴Biological Engineering Program, Faculty of Engineering, King Mongkut's University of Technology Thonburi, Bangkok, Thailand

⁵Global Chemical Co., Ltd. Bangpoo Industrial Estate, Samutprakarn, Thailand

⁶Department of Physical Science, Faculty of Science, Prince of Songkla University, Hat-Yai, Thailand

⁷Department of Physics, Rajarajeswari College of Engineering, Bangalore, India

⁸Center for Lightweight Materials, Design, and Manufacturing, Department of Mechanical Engineering, Faculty of Engineering, King Mongkut's University of Technology Thonburi, Bangkok, Thailand

Received 28 April 2022; accepted in revised form 16 July 2022

Abstract. Natural rubber (NR) composite foam was developed through the Dunlop process with better volatile solvent absorption and antibacterial activity. The unmodified and modified titanium dioxide (TiO₂), namely TiO₂-zinc oxide (TiO₂-ZnO) and TiO₂-silver doped zirconium (TiO₂-Ag-Zr), were incorporated into the foams. The photocatalytic origination under UV and visible light leads the composite foam with TiO₂-ZnO to exhibit effective and suitable benzene absorbing and removing abilities. Thus, the specific foam sizes provided the gaseous benzene absorption of 14.0 ppm within 3 h and the gaseous benzene elimination of 7.6 ppm within 14 h in case of the composite with 10 phr TiO₂-ZnO. Also, the foams with NR/TiO₂-ZnO and NR/TiO₂-Ag-Zr exhibited excellent antibacterial activity for *E. coli* due to the release of Zn⁺ and ROS species across the rubber foam filter layers to the bacteria surfaces. The resulting composite foam showed superior elastic properties in terms of tensile strength, toughness, and elongation at break. To study the applicability as filter, the engineering simulation relating the air flowability throughout the foam was examined. From the flow velocity and the air permeability of the foam at a specified thickness, it was observed that the NR/TiO₂-ZnO exhibited proper porous sizes and shapes for filtering, reacting, absorbing and removing the gaseous benzene relative to other porous filters.

Keywords: nanocomposites, rubber, modified titanium dioxide, mechanical properties, photocatalytic properties

*Corresponding author, e-mail: yeampon.nak@kmutt.ac.th

© BME-PT

1. Introduction

Environmental pollution is one of the major issues that need to be reduced. Air pollutants are the problems that severely affect human health, including particulate matters, biological molecules and gases, particularly volatile organic compounds (VOC). These chemical pollutants disperse in the air and have adverse health effects on humans in both the short and long term [1]. VOC emission sources are numerous and widespread, including outdoor and indoor sources such as vehicle exhaust, gas stations, solvent-coated furniture, cleaning devices, cooking, cigarette smoke and *etc.* In addition, during the endemic situation in recent years has been realized that biological pollutants, especially pathogenic types including bacteria, fungi, and viruses, affect human health. These microorganism infections cause illnesses, either mild or severe life-threatening infections in humans. The pathogen as an infectious agent can spread into the human body through contaminated food or water, inhaling particles or droplets, and contact with contaminated objects. As a result, physical adsorption and chemical treatment methods have been applied to resolve the spreading of pollutants [2, 3]. However, the procedure to eliminate both the chemical and biological matters simultaneously is required.

Advanced oxidation processes (AOP) is a chemical treatment that produces strong oxidizing agents to degrade organic contaminants continuously to small organic molecules or harmless products, including organic volatile, dyes as well as microorganisms [4]. These processes include Fenton reaction [5], photocatalysis [6], and ozone oxidation [7]. Photocatalysis has been widely employed for pollutant treatment using ultraviolet (UV) irradiation to activate semiconductor material for generating reactive species (ROS) such as hydroxyl radical ($^{\bullet}\text{OH}$), hydroperoxyl radical ($^{\bullet}\text{OOH}$), superoxide anion ($^{\bullet}\text{O}_2^-$) and hydrogen peroxide (H_2O_2) to oxidize organic substances [8]. Semiconductor materials such as titanium dioxide (TiO_2) [9], zinc oxide (ZnO) [10], stannous oxide (SnO) [11], tungsten trioxide (WO_3) [12], and iron oxide (Fe_2O_3) [13] and *etc.* have been intensively investigated due to their photocatalytic behaviors.

TiO_2 is the most widely used material that acts as a photocatalyst due to its energy band gap sufficiently absorbing UV irradiation, biologically and chemically inert nature, corrosion resistance, non-toxicity, and inexpensive [14]. TiO_2 is a highly efficient

photocatalysis that excites electrons from the valence band to the conduction band and creates electron-hole pairs (e^-h^+). This phenomenon further originates from the reaction to the oxygen and water molecules and produces strong oxidizing agents of $^{\bullet}\text{OH}$, H_2O_2 and $^{\bullet}\text{O}_2^-$ [14]. These oxidizing agents can break down the organic compounds to reduce their harmfulness like water and carbon dioxide. TiO_2 photocatalyst has been applied in various fields such as air pollutant treatment, wastewater treatment disinfection purpose and self-cleaning [9, 14, 15]. However, the major drawback of TiO_2 is its large energy band gap of 3.0–3.2 eV and it absorbs photons only in the range of UV irradiation. Hence, this inactive nature of TiO_2 under the visible light region leads to a limitation for indoor application. Also, the recombination of electron-hole pairs during the photocatalytic reaction is another limitation of photocatalytic efficiency. To enhance the photocatalytic efficiency under the visible region and reduce the charge recombination, modification of TiO_2 structure in order to shift the electronic band need to be investigated. However, there are several strategies to modify TiO_2 , including coupling with other semiconductors [16], doping with metal [17], or non-metal ion [18], codoping with two or more ions [19], and noble metal nanoparticle deposition [20]. The improved photocatalytic performance of TiO_2 reduces the band gap and electron-hole pair recombination extends the application to wastewater degradation, gaseous elimination and microbial inactivation under UV and visible regions.

However, TiO_2 cannot be used in powder form for applications due to its ease of release during usage, difficulty in recovering the catalyst, and high cost to reuse [21]. Thus, the incorporation of TiO_2 powder into the supporting matrix is an important factor in extending its application in numerous fields, especially in rubber products. In rubber industries, TiO_2 is normally used as semi-reinforcing filler and white pigment to color rubber products. In addition, photocatalytic properties of TiO_2 are distinctive beyond other fillers like silica, carbon black, clay, and calcium carbonate, which do not have such properties. Incorporation of TiO_2 into rubber film has been reported to improve mechanical, dye adsorption, and antimicrobial properties [22, 23]. However, the film has the disadvantage of restricting the activity of TiO_2 in the matrix as they are covered with rubber molecules, and it retards the electron transfer

through the layers of the rubber matrix. Therefore, the porous structure of the composite induces a large surface area which is very important for photocatalytic activity [22]. The addition of TiO_2 in rubber composite foam can improve the attraction between the surface of composites and organic pollutants by improving the efficiency of eliminating methylene blue (MB) and gaseous benzene under UV irradiation [24]. However, the photocatalytic activity of composite foam is limited under UV light; the incorporation of modified TiO_2 in the rubber composite foam is investigated synergistically the photocatalytic behavior like volatile elimination and antibacterial activity can be applied in case of indoor and outdoor rubber foam products. Among several rubber types, the natural rubber (NR) is widely used in various applications regarding its superhydrophobic and insulative properties, elasticity, flexibility and biological resources. This serves several chances for the incorporation of the TiO_2 to improve the distinguished properties of NR products such as conductive composite [25, 26], photocatalyst and disinfectant materials [24]. This is a promising and challenging study in the field of rubber technology since there are no prior works to examine clearly the phenomenon of TiO_2 in rubber matrix foam.

Therefore, in the present work, rubber foams based on NR/ TiO_2 composites were prepared using the Dunlop process. Three types of TiO_2 were used in the forms of pure TiO_2 , modified TiO_2 with ZnO (TiO_2 -ZnO), and modified TiO_2 with silver and zirconium (TiO_2 -Ag-Zr). It is noted that each TiO_2 has different crystalline structures, energy band gap, particle size and morphology. It is proposed to clarify the photocatalytic activity of different types of TiO_2 . Degradation of MB solution and benzene gas were used to evaluate the activities of the resulting composite foams under UV and visible light conditions. The reinforcement efficiency of TiO_2 particles in the NR foam matrix can be elucidated based on the variation in mechanical properties. The antibacterial property of the composite foams was illustrated using *Escherichia coli* (*E. coli*) as a representative of gram-negative bacteria, which is the most common bacterial species responsible for human pathogens [27]. It causes various infections, including cholecystitis and cholangitis, peritonitis, cellulitis, osteomyelitis, and nosocomial pneumonia [28]. The transmission of bacteria to humans occurs through the contamination of hands or objects. Also, the air

flowability through the complex foam structure was examined together with the engineering simulation, and the air permeability was evaluated following the Darcy's law for studying the possibility of using the foam as the natural foam filter.

2. Experimental section

2.1. Materials

High ammonia concentrated natural rubber latex (HA-NR) with 60% dry rubber content (DRC) was manufactured by Num Rubber & Latex Co., Ltd. (Trang, Thailand). Potassium oleate (K-oleate), sulfur, zinc 2-mercaptobenzothiazone (ZMBT), zinc diethylthiocarbonate (ZDEC), Lowinox CPL (butylated reaction product of para-cresol and dicyclopentadiene), zinc oxide (ZnO), diphenyl guanidine (DPG) and sodium silicofluoride (SSF) were purchased from Thanodom Trading Co., Ltd. (Bangkok, Thailand). Pure TiO_2 and modified TiO_2 with ZnO (TiO_2 -ZnO) powders were supplied by Global Chemical Co., Ltd. (Samut Prakan, Thailand) and modified TiO_2 with a silver (Ag) and zirconium (Zr) (TiO_2 -Ag-Zr) were in-house produced as stated elsewhere [19]. Three types of TiO_2 powders were well ground using ball milling at 25 °C for 72 h. The average particle sizes of the pure TiO_2 , TiO_2 -ZnO and TiO_2 -Ag-Zr suspension are reported as 0.71, 0.55 and 0.49 μm , respectively, following the measure from the Light scattering particle size analyzer (HORIBA, LA600, Kyoto, Japan).

2.2. Preparation of NR composite foams

The NR composite foams were prepared through the Dunlop process. All ingredients and their concentrations in the composite foam are shown in Table 1. The process was initiated from the incorporation of K-oleate soap, sulfur, ZMBT, ZDEC, Lowinox CPL and pure TiO_2 or TiO_2 -ZnO or TiO_2 -Zr-Ag dispersions into HA-NR latex in the food mixer (Kitchen Aid, Michigan, USA). The mixture was stirred at a mixing speed of 80 rpm for 4 min. The mixing speed was then increased to 180 rpm and stirred continuously for 4 min until the volume of the foam increased up to approximately three times the initial volume, and further, the speed was reduced to 80 rpm for 1 min. The mixing was continued for another 1 min upon the addition of DPG and ZnO, and finally added gelling agent of SSF for 30 s primarily before transferring the mixture into a glass mold at room temperature to allow gel formation. The gelled

Table 1. Formulation for the preparation of composite foams filled with different types of TiO₂.

Ingredients	Chemical roles	Contents [phr]
60% HA-NR latex	Rubber matrix	100.0
20% Potassium oleate	Surfactant	1.5
50% Sulfur	Vulcanizing agent	2.0
50% ZMBT	Primary accelerator	1.0
50% ZDEC	Secondary accelerator	1.0
50% ZnO	Activator	3.0
50% Lowinox CPL	Antioxidant	1.0
50% DPG	Secondary gelling agent	1.0
20% SSF	Primary gelling agent	1.0
30% Pure TiO ₂	Filler	0–20
30% TiO ₂ -ZnO	Filler	
30% TiO ₂ -Ag-Zr	Filler	

foam was vulcanized in a steam curing system for at least 40 min. The vulcanized foam was washed with water to eliminate the excessive chemicals and dried in a hot air oven at 70 °C for 24 h [24].

2.3. Characterization of the molecular structure of TiO₂

2.3.1. X-ray diffractometer (XRD)

The crystalline structures of pure TiO₂, TiO₂-ZnO and TiO₂-Ag-Zr powders were analyzed by XRD technique (XPert MPD, Philips X' Pert MPD, Almelo, Netherlands) with Cu K α irradiation source. The XRD pattern in the 2 θ range of 20–80 degrees was recorded.

2.3.2. X-ray photoelectron spectrometer

The elemental positions and chemical states of pure TiO₂, TiO₂-ZnO and TiO₂-Zr-Ag powder were analyzed by XPS (Kratos Analytical Axis Ultra, UK). The samples were analyzed by using a monochromatic Al K α X-ray source. Wide scan spectra in the range of binding energy of 0–1200 eV were reported.

2.3.3. Ultraviolet-visible-near infrared (UV-VIS-NIR) spectrometer

The absorbance spectra of TiO₂, TiO₂-ZnO and TiO₂-Zr-Ag samples were characterized by UV-VIS-NIR spectrophotometer (Shimadzu SolidSpec-3700, Kyoto, Japan) at the wavelength range of 200–800 nm. The energy band gap of all samples was determined by the cut-off wavelength of the UV-visible absorbance spectrum by using the Tauc plot method.

2.3.4. Transmission electron microscope (TEM)

The morphology of TiO₂, TiO₂-ZnO and TiO₂-Zr-Ag particles were analyzed by transmission electron microscope (TEM) (Model JEOL, JEM-1400, Tokyo, Japan) operated at 80 kV accelerating voltage. The powder specimen was dispersed in ethanol and sonicated for 30 min, then dropped on the carbon-coated copper grid until the solvent evaporated completely before analysis.

2.4. Characterization of NR/TiO₂ composite foams

2.4.1. Tensile properties

Tensile properties of the foams were measured using a low force electromechanical universal testing machine (model 3365, Instron[®] Inc., Massachusetts, USA). The Dumbbell shape specimens were prepared according to ISO 37 Type 2, and the load was varied at a crosshead speed of 200 mm/min. Modulus at 100% elongation, tensile strength, and elongation at break of the foam were reported.

2.4.2. Morphologies

The surface morphology study of the composite foam was carried out using scanning electron microscope (SEM), (Apreo, Thermo Fisher Scientific, Brno, Czech Republic) equipped with a dispersive energy X-ray (EDX) detector to observe the nature of dispersion of the unmodified and modified TiO₂. The foam surface was sputter-coated with gold under vacuum prior to being characterized by SEM.

2.4.3. Air permeability

Measurement of air permeability of the composite foam was performed by air permeability tester (Mesdan Lab 3240B, England). The air flow vertically through the specimen of 5.0×5.0 cm² at a pressure of 500 Pa was measured.

2.5. Photocatalytic degradation of MB

MB represents the organic dye to determine the photocatalytic efficiency of composite foam under UV and fluorescent irradiation. The samples of 3.0×3.0×0.2 cm³ were prepared using the in-house fast-cutting machine and immersed in 60 ml of 10⁻⁵ M of MB solution under the dark condition at room temperature until the adsorption equilibrium has reached (approximately 10 days). Then, it was exposed to UV irradiation (15 W UV-C lamp) and

fluorescent irradiation (15 W fluorescent lamp). 2 ml of MB solution was taken and the spectra were recorded for 2, 5, 8, 12, 16, 20 and 24 h of time by using a UV-visible spectrophotometer (GENESYS 10-S, Massachusetts, USA). The photocatalytic activity of composite foams was observed from the reduction in intensity at the maximum wavelength ($\lambda_{\max} = 664$ nm) and the percentage of photodegradation efficiency (\varnothing_p) to degrade MB was calculated as Equation (1) [29]:

$$\varnothing_p [\%] = \frac{C_0 - C}{C_0} \cdot 100 \quad (1)$$

where C_0 is the initial concentration of MB solution and C refers to the concentration of MB solution at a time t .

2.6. Photocatalytic degradation of gaseous benzene

The foams filled with unmodified and modified TiO₂ exhibited the highest photodegradation efficiency of MB solution is the intention of evaluating the gaseous benzene degradation. The experiment was carried out in a closed stainless-steel reactor by using a volumetric batch of size 54 l. The reactor has equipped two blowers, and two 20 W LED lamps to maintain the visible irradiation condition. The foam sheet (28.0×28.0×0.2 cm³) was kept inside the reactor. Then, the benzene gas with a concentration of 100 ppm (19.7 μl) was injected into the reactor. The specimen was placed in the dark condition until the foam adsorption reached equilibrium before turning on the lamp. Further, 1 ml of gaseous benzene was sampled for every 1 h. The concentration of gaseous benzene was eventually measured using a gas chromatography/flame ionization detector (GC/FID) (Shimadzu GC-14B, Tokyo, Japan) with a set-up of the injection temperature of 100 °C, column temperature of 100 °C and detection temperature of 150 °C.

2.7. Antibacterial property

The antibacterial property of the composite foam was investigated using *Escherichia coli* (*E. coli*) carrying pSB2K3-mCherry plasmid (mCherry red fluorescent protein or mCherry) as a representative of gram-negative bacteria has been used for the qualitative analytical method. The qualitative determination of antibacterial testing was carried out by the

zone inhibition test. A single colony of the *E. coli* was inoculated under aseptic conditions in Luria Broth (LB) medium and incubated at 37 °C for 18 h in an incubator shaker. Further, 100 μl of 1·10⁸ CFU/ml bacteria suspension was added and spread onto an LB agar plate containing 50 μg/ml kanamycin. Composite foams with the size of 10×10 mm² were sterilized by autoclaving, placed onto the plates, and incubated at 37 °C for 24 h in an incubator. The antibacterial property of the composite foam was assessed by measuring the clear inhibition zone observed around the specimen [30].

2.8. Micro-computed tomography (μCT)

The 3D morphologies of the composite foams were examined using high-resolution μCT, the Bruker SkyScan 1173 (Bruker Corporation, Massachusetts, USA). μCT allows the assessment of both external and internal features of the samples [31]. Scanning was performed by using an X-ray source with an operating voltage 130 kV and a current of 61 mA. The resolution of the μCT scan mainly depends on the voxel size. Although smaller voxel sizes provide finer geometrical details, it also leads to a significant increase in total scanning time. The voxel size of 20 μm was adopted in the present study. Upon the completion of the CT scan, a series of 2D images were obtained. The three-dimensional images were obtained by incorporating the two-dimensional images, and it was performed by the ScanIP (Simpleware Ltd., Exeter, UK) [32].

3. Results and discussion

3.1. Molecular structure of unmodified and modified TiO₂

The molecular structure of three TiO₂ types are analyzed using XRD technique in order to determine their crystal structures, as shown the diffraction patterns in Figure 1. The diffraction peaks of unmodified TiO₂ at 25.35, 37.82, 48.06, 53.91, 55.08 and 62.90° are attributed to the crystalline planes of (101), (004), (200), (105), (211) and (204), respectively. These are comparable to the Joint Committee on Powder Diffraction Standards database (JCPDS card No 21-1272) [19]. It indicates that the structure of unmodified TiO₂ is similar to the anatase structure. The characteristic patterns of anatase-TiO₂ are also present in all the specimens. In addition, the XRD pattern of modified TiO₂ with ZnO (TiO₂-ZnO) shows the peaks at 31.87, 34.45, 36.29, 56.64,

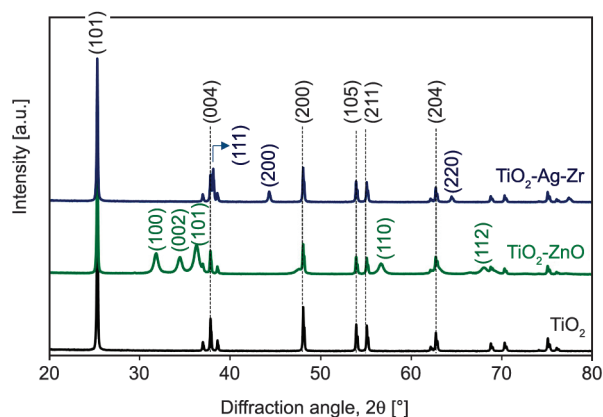


Figure 1. XRD patterns of TiO₂, TiO₂-ZnO and TiO₂-Ag-Zr particles.

67.91° corresponds to the planes of (100), (002), (101), (110), (112) (JCPDS card No.36-1451) [33], indicating the hexagonal wurtzite structure of ZnO. Considering the diffraction peaks of modified TiO₂ with Ag and Zr (TiO₂-Ag-Zr), it shows the characteristic peaks of Ag at 38.12, 44.29 and 64.43° owing to the planes (111) and (200) and (220), respectively [34]. Also, the peak of Zr is expected at 32.61° (020) and 30.2° (111); however, due to the less concentration of Zr and non-uniform dispersion inside the TiO₂, the peak has not been distinguished [19]. The

crystalline size of TiO₂, ZnO and Ag nanoparticles was determined through the Scherrer equation [19] by using the Equation (2):

$$D = \frac{0.9\lambda}{\beta \cos \theta} \quad (2)$$

where *D* is the crystalline size, *λ* is the wavelength of X-ray (0.1540 nm), *β* is full width at half maximum (FWHM) corresponding to XRD peaks and *θ* is the angle of diffraction. The crystallite size of three types of TiO₂ powder exhibited the crystallite sizes of anatase-TiO₂ phase of 62.64 nm, 26.90 nm for ZnO nanoparticles and 55.85 nm for Ag nanoparticles.

The elemental composition and chemical bonding of unmodified and modified-TiO₂ are analyzed by X-ray photoelectron spectroscopy (XPS), as shown in Figure 2. All specimens exhibit the signals of Ti 2p and O 1s elements assigned to Ti–O bonds in TiO₂ crystal lattice. The characteristic signals of Ti 2p show two peaks at 464 and 458 eV, indicating the 2p_{1/2} and Ti 2p_{3/2} states of Ti⁴⁺ ions in anatase TiO₂, respectively (Figure 2b). This is favorable for the formation of electrons and hole in TiO₂ during photocatalytic reaction under UV irradiation [35]. In addition, the C 1s contaminant is observed at 284 eV

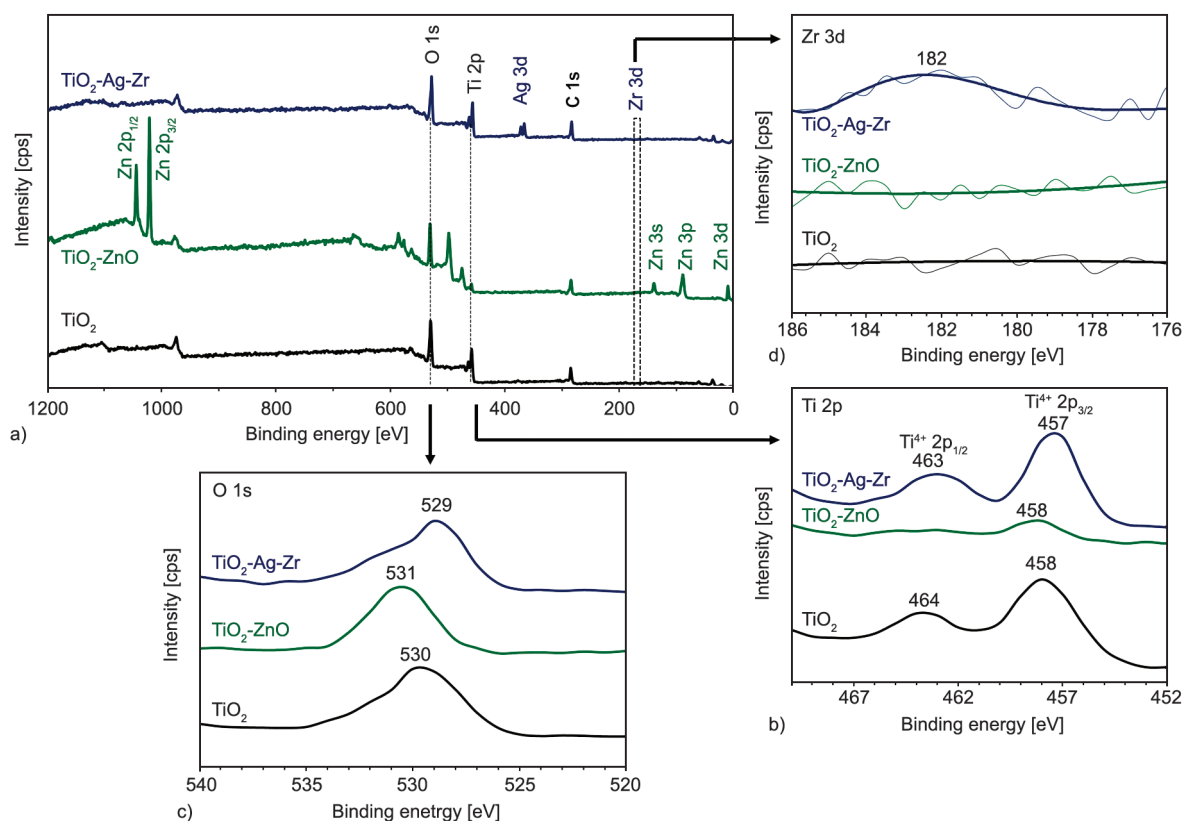


Figure 2. XPS spectra of TiO₂ and its modified forms (a), spectra of Ti 2p peaks (b) spectra of O 1s peaks (c) and spectra of Zr 3d (d).

due to the presence of residual organic precursors. However, the spectrum of modified TiO₂ exhibits new characteristic peaks. Modified TiO₂ with ZnO shows two sharp peaks at 1021 and 1044 eV attributed to Zn 2p_{3/2} and Zn 2p_{1/2} states of Zn²⁺ ions. The Ti 4⁺ signals are located at 458 and 464 eV (Figure 2b), it does not show any shift of binding energy when compared to the unmodified TiO₂. It indicates the coexistence of TiO₂ and ZnO in the deposited form of ZnO nanoparticles on the TiO₂ surface. The incorporation of ZnO nanoparticles decreases the peak intensity of Ti 2p, while O 1s signal intensity has not changed (Figure 2c) due to the formation of Ti–O bonds in TiO₂ and Zn–O bonds in ZnO crystal lattices. In the case of TiO₂-Ag-Zr, the signal peak of Ag element on TiO₂ surface located at 373 and 367 eV is assigned to Ag 3d_{3/2} and Ag 3d_{5/2} states of Ag⁺ ions [29]. The signal at 182 eV shows a small peak of Zr atom attributing Zr 3d_{5/2} state of Zr⁴⁺ ion as seen in Figure 2d. The shifting of Ti 2p and O 1s peaks to lower binding energy is observed in Figure 2b and Figure 2c. It is noted that, under calcination conditions, Zr⁴⁺ ions were incorporated into the TiO₂ lattice due to the ionic radius of Zr⁴⁺ (0.072 nm) is similar to Ti⁴⁺ (0.065 nm), leading to the substituting of Zr⁴⁺ ions in the structural defect of TiO₂ such as vacancies in its lattice [19, 36]. While ionic radius of Ag is 0.128 nm which has larger than Ti ion leading to the deposition of Ag particles on the TiO₂ surface as proposed in the TEM image in Figure 4. In order to assess the ability to eliminate the organic substance under UV and visible regions, UV-visible absorbance spectra and estimated energy band gap of unmodified and modified TiO₂ are presented in Figure 3. The three types of TiO₂ show strong absorption of UV radiation in the range of 200–400 nm.

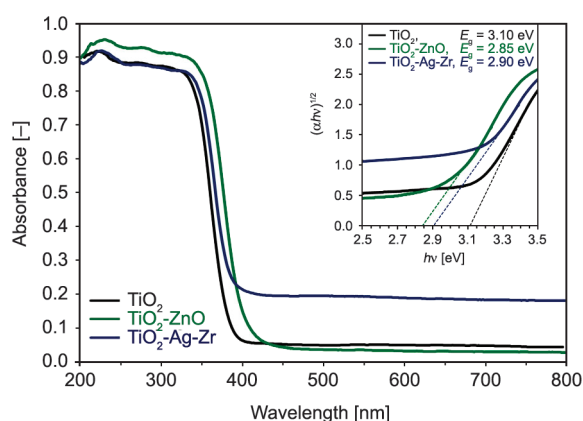


Figure 3. UV-visible absorbance spectra of TiO₂, modified TiO₂ with ZnO and modified TiO₂ with Ag-Zr.

Unmodified TiO₂ shows less absorption in the range of the visible light region. The modified TiO₂ with ZnO reveals the shifting of absorbance spectra to the longer wavelength region when compared to the one without modification. Also, the spectra of TiO₂-Ag-Zr slightly shift to the higher wavelength due to the replacement of Zr⁴⁺ in the TiO₂ lattice [19, 36]. This is in good agreement with the shifting of Ti 2p in XPS (Figure 2b). A strong absorption during visible irradiation in the range of 400–800 nm is observed because of the surface plasmon resonance effect, which is the characteristic optical property of Ag nanoparticles [37]. The absorption spectrum shifts towards the longer wavelength indicating the decrease in the energy band gap of TiO₂, determined by the Tauc plot method as presented in the inset of Figure 3. The absorption coefficient $(\alpha h\nu)^{1/2}$ and photon energy $h\nu$ are plotted. The intercept on the x-axis of the linear fit of the Tauc plot curve is the estimated band gap [38]. It can be seen that the band gap is reduced from 3.1 eV of unmodified TiO₂ to 2.85 eV and 2.90 eV of TiO₂-ZnO and TiO₂-Ag-Zr, respectively. It indicates that the modified forms of TiO₂ with ZnO nanoparticles and co-doped Ag-Zr elements significantly reduced the band gap of pure TiO₂. Thus, the modification of TiO₂ induces electron movement and enhances the oxidizing efficiency in the photocatalytic process under UV and visible light irradiation.

To support the modification of TiO₂, the TEM micrographs of both unmodified and modified TiO₂ powder are imaged and presented in Figure 4. It is seen that the unmodified TiO₂ exhibits agglomeration of spherically shaped particles with a diameter of 75–180 nm, as shown in Figure 4a. For the modified TiO₂ with ZnO (Figure 4b and 4c), agglomeration of ZnO nanoparticles is found around the TiO₂ surface with a diameter of approximately 10–20 nm. The modified TiO₂ with co-doped Ag and Zr elements exhibited the spherical Ag nanoparticles deposited on the surface of TiO₂ (Figure 4d and 4e). The particle size of Ag nanoparticles is in the range of 10–30 nm. It supports the intensity of XRD peaks and XPS spectra as well as the surface plasmon effect in the UV-visible absorbance spectrum. Whereas Zr elements are possibly doped into TiO₂ lattice during calcination process could not be distinguished on TiO₂ surface [39]. However, the existence and distribution of Ag and Zr elements in the modified TiO₂ were determined using an energy dispersive

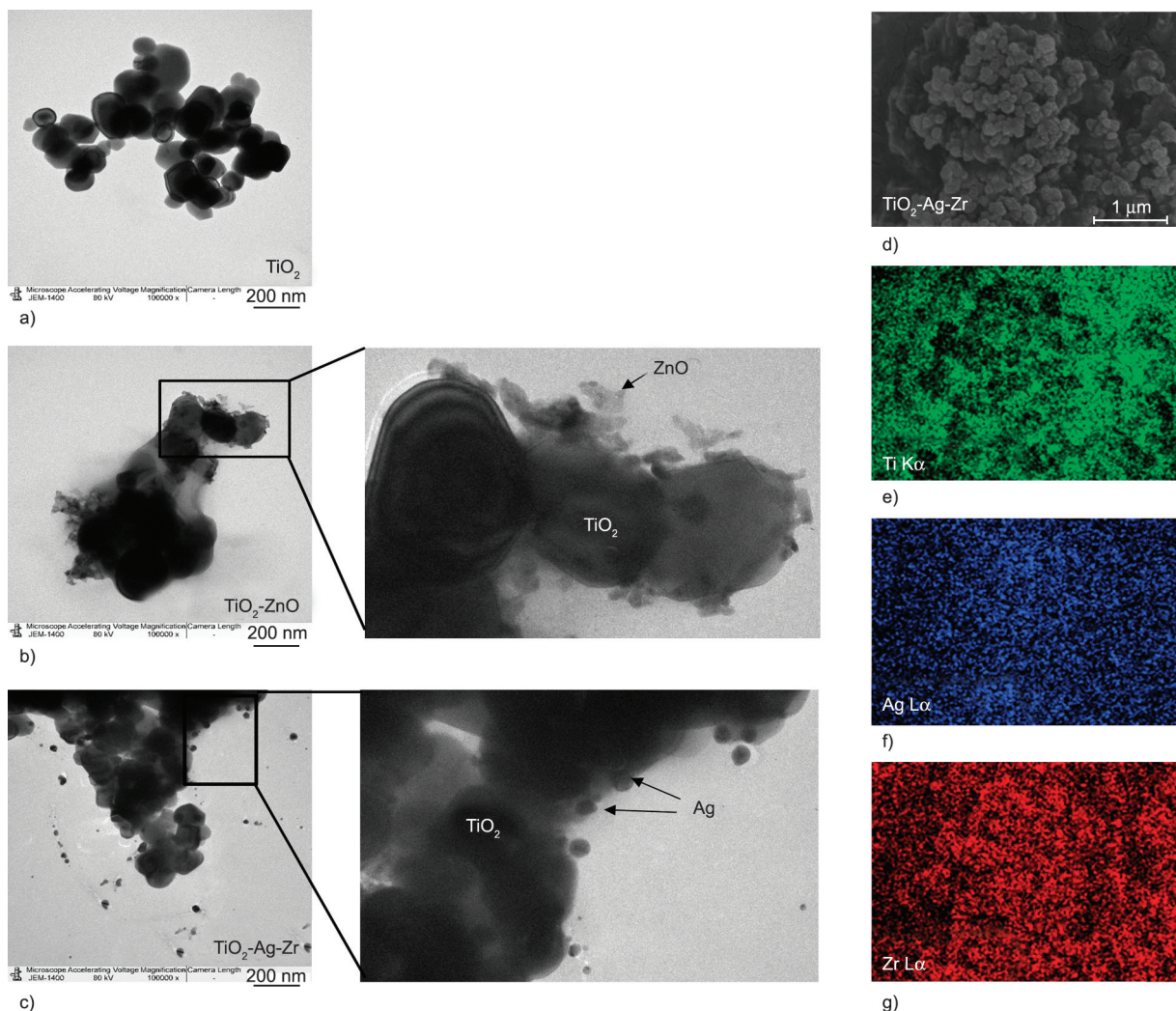


Figure 4. TEM images of TiO₂ (a), TiO₂-ZnO (b), TiO₂-Ag-Zr (c) particles and SEM-EDX image of TiO₂-Ag-Zr (d) particles through the Ti (e), Ag (f) and Zr (g) atoms detection.

X-ray analysis (EDX), as shown in Figure 4d–4g. The Ag L α and Zr L α signals were randomly dispersed in TiO₂-Ag-Zr particles. Modification of TiO₂ by dispersing ZnO nanoparticles and co-doping with Ag and Zr elements extended the photo-response of TiO₂ to the visible region relating a shift of absorption spectrum to longer wavelength compared to the unmodified TiO₂ as shown in Figure 3. Based on these results, it can be summarized that modification of TiO₂ with ZnO nanoparticles and doping Ag and Zr elements enhances the ability to eliminate organic substances via photocatalytic process under UV and visible light exposure. Three types of TiO₂ were added to the NR latex to prepare the composite foam. The photocatalytic efficiency of the composite is assessed from the degradation of MB solution and gaseous benzene, while the reinforcement efficiency, air permeability, and antibacterial properties of TiO₂-filled NR composite foam

are also examined in order to check the feasibility of using the foam as a filter.

3.2. Photocatalytic degradability via the photocatalytic process

Photocatalytic activity of the composite foam with varying unmodified and modified TiO₂ concentration is determined based on the degradation of MB solution under fluorescent and UV light conditions. The degraded MB solution is measured by a UV-visible spectrophotometer at a wavelength of 664 nm. Figure 5 shows the photodegradation efficiencies of the composite foams after exposure of UV light. It is found that the degradation of dye solution is significantly increased upon increasing the irradiation time after adding the three types of modified TiO₂. Here, the maximum TiO₂ concentration for MB degradation measurement is noticed at 10 phr. NR composite foams filled with 10 phr of unmodified

TiO₂ show 70% MB degradation upon exposure of UV light for 24 h (Figure 5a). However, the incorporation of TiO₂-ZnO and TiO₂-Ag-Zr in the composite foam shows more efficiency than the one with unmodified TiO₂. The addition of TiO₂-ZnO provides 90% MB degradation, while TiO₂-Ag-Zr exhibits 85% of MB degradation on exposure to UV light for 24 h. It has to be noted that the increase of TiO₂-ZnO content above 10 phr is not practical due to the flocculation of foam during processing. The presence of unmodified and modified TiO₂ in the composite foam produces electron-hole pairs (e_{cb}^- , h_{vb}^+) on the photocatalyst surface under UV irradiation. The e_{cb}^- in the conduction band reacts with oxygen (O₂) to produce superoxide radicals (O₂^{•-}) and

reduces to hydroxyl radical (OH[•]), while the h_{vb}^+ in the valence band oxidizes with water molecules in the aqueous solution to form OH[•]. The OH[•] species are recognized as highly reactive radicals to degrade organic dye compounds. In the case of TiO₂-ZnO, the nanoparticles of TiO₂ and ZnO are semiconductors with a similar energy band gap, which is enough to induce the formation of e_{cb}^- - h_{vb}^+ pairs. In the case of TiO₂-Ag-Zr, e_{cb}^- is excited to the conduction band of TiO₂ before transferring to the Ag nanoparticle, which acts as the electron trapping, enhances the electron-hole pair separation, and produces the reactive species based on the trapping of the electron with O₂ [19]. Thus, the addition of modified TiO₂ improves the photocatalytic activity

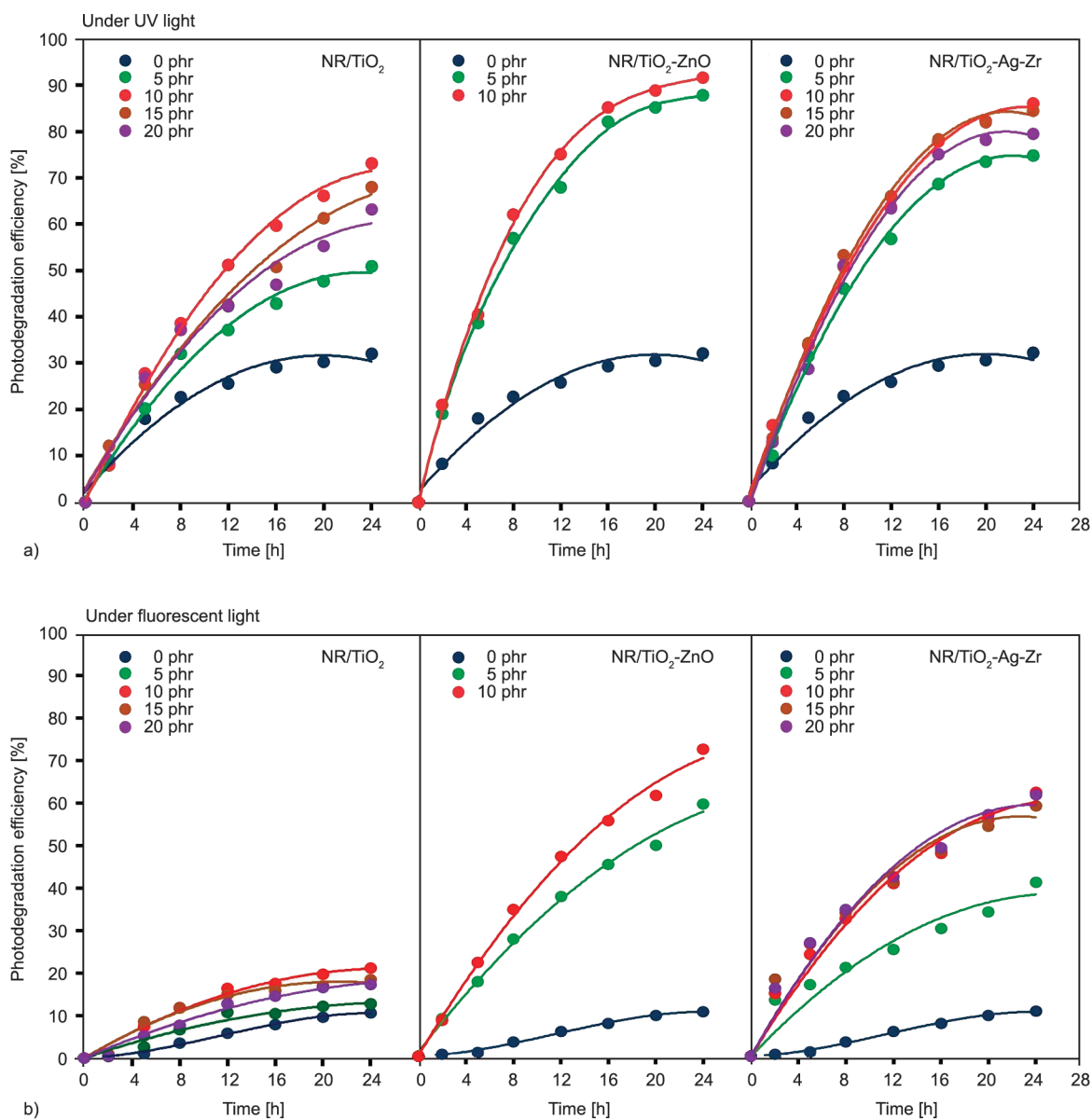


Figure 5. Photodegradation efficiency of the composite foams filled with TiO₂, TiO₂-ZnO and TiO₂-Ag-Zr under UV (a) and fluorescent (b) light for 24 h.

of NR composites in order to degrade the organic dye substance.

The photodegradation efficiency of composite foams to the degraded MB solution after exposure to the fluorescent light is shown in Figure 5b. MB solution containing composite foam filled with unmodified TiO₂ shows a small change in the efficiency upon increasing the irradiation time. In addition, an increase in the amount of unmodified TiO₂ to 10 phr displays optimum degradation of MB solution of 20% upon the exposure of fluorescent light for 24 h. It indicates that the wide energy band gap of TiO₂ at 3.10 eV is not sufficient to produce oxidizing agent in the photocatalytic process under visible irradiation. In contrast, the NR foams incorporated with TiO₂-ZnO and TiO₂-Ag-Zr reduce the MB concentration by increasing the irradiation time. Also, the efficiency is increased with increasing photocatalyst concentration to 10 phr. These results prove that the modification of TiO₂ enhanced the photocatalytic activity of the composite under the visible light region. However, two types of modified TiO₂ show different photodegradation degrees due to the difference in band gap structures. The NR composite foam filled with TiO₂-ZnO exhibits higher photodegradation than that of TiO₂-Ag-Zr. The addition of 10 phr TiO₂-ZnO reduces the MB concentration up to 70%, while the foam incorporated with of TiO₂-Ag-Zr shows 60% after exposure to fluorescent light for 24 h. According to the results, modified TiO₂ has strong efficiency in degrading well the organic dye substances under visible light, and it can be described with the help of the proposed model as shown in Figure 6. In the case of TiO₂-ZnO, generally TiO₂ ($E_g = 3.10$ eV) and ZnO ($E_g = 3.26$ eV) [40] are having similar energy band gap, leading to their efficiencies to excite the electron under UV light. However, the ZnO nanoparticles deposited on the TiO₂ surface form heterojunctions is an advantage for the excitation of charges under visible light as shown in Figure 6a. When it is exposed to visible light, e_{cb}^- of the lower energy gap of TiO₂ will be excited to the interface of the conduction band of ZnO. Then, the e_{cb}^- in the conduction band of ZnO also transfers to the conduction band of TiO₂, while h_{vb}^+ in the valence band of TiO₂ moves to the valence band of ZnO [41]. These behaviors promoted the decrease of the energy band gap, prevented the e_{cb}^- and h_{vb}^+ recombination, and increased the lifetime of the charge carrier by enhancing the reaction between reactive hydroxyl radicals and organic

dye molecules. This mechanism indicates that a greater number of reactive species is found under UV irradiation from both TiO₂ and ZnO, relating to the higher degradation of MB solution when compared to the case of visible light. However, the modification of TiO₂-ZnO improves the photocatalytic activity under visible light, while the one with unmodified TiO₂ shows low activity. The foam with TiO₂-Ag-Zr, provides synergistic effects as seen in the improved photocatalytic reaction, as shown in the proposed model (Figure 6b). Doping of Zr element in TiO₂ lattice reduces the energy band gap of TiO₂, leading to the ease of e_{cb}^- excitation from the valence band to conduction band. The functional Ag nanoparticles deposited on the TiO₂ surface act as a surface trap that captures the electron transferring from the conduction band of TiO₂ [42]. In addition, the surface plasmon resonance characteristics of Ag nanoparticles facilitate to creation charge carrier under the visible region [43]. The e_{cb}^- generated from Ag nanoparticles can transfer to the conduction band of TiO₂ [19]. The movement of e_{cb}^- from TiO₂ and Ag nanoparticles assists retarding the electron-hole recombination. The reaction of $h\nu_{vb}^+$ in the valence band with H₂O and e_{cb}^- with O₂ under visible conditions induces the creation of a strong reactive radical of OH[•] species, resulting in considerable degradation of MB organic dye. The possible mechanism of OH[•] with MB solution is also proposed in Figure 6c. The three possibilities of MB degradation are generated through *N*-demethylation (Figure 6(i)), cleavage of thiazine group (–C=N- and –C=S-bonds) (Figure 6(ii)) and additional reaction of hydroxyl (–OH) and carbonyl (C=O) groups (Figure 6(iii)) [44, 45].

To express the photocatalytic ability of the foam, the kinetics of the photocatalytic degradation rate of MB solution is based on the Langmuir Hinshelwood kinetics [46] using Equation (3):

$$\ln \frac{C_0}{C} = kt \quad (3)$$

where C_0 and C are the initial concentration and the concentration during measurement, k is the pseudo-first-order rate constant obtained from the slope of $\ln(C_0/C)$ versus irradiation time (t) plots.

Variations of the calculated photocatalytic degradation rates of the composite foam under UV and visible light conditions are summarized in Table 2. The rate constants for degrading MB by the composite foam filled with three different types of TiO₂ are

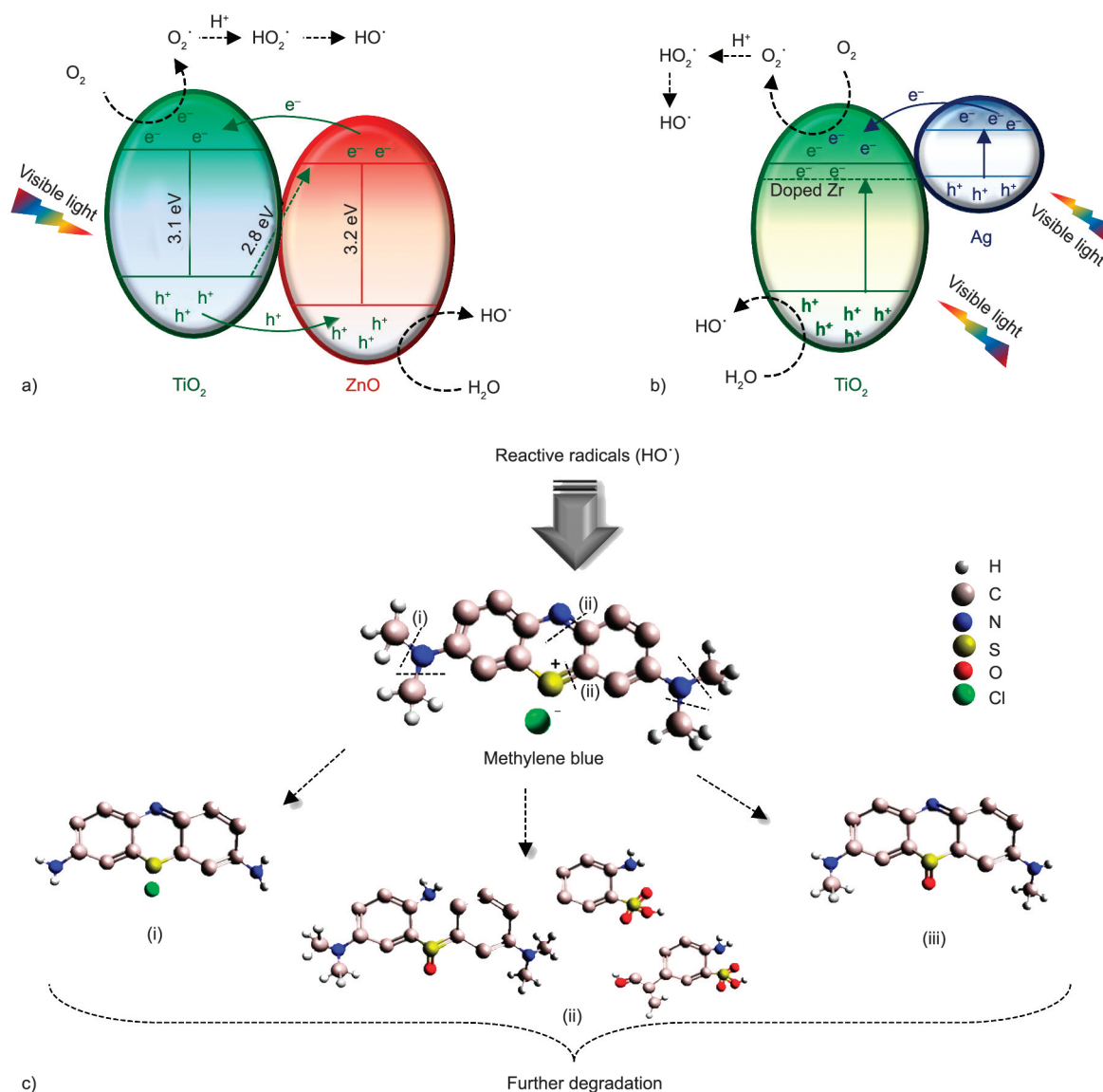


Figure 6. Proposed mechanism of the photocatalytic reaction of TiO₂-ZnO (a), TiO₂-Ag-Zr (b) and proposed mechanisms of the photocatalytic reaction (c) for degradation of MB under visible irradiation.

found to be increased upon increasing the concentration of TiO₂ up to 10 phr under both UV and visible light. Above 10 phr, the rate constants (*k*) are decreased due to the agglomeration of TiO₂ in the composite. In case of different TiO₂, the foam with

10 phr of TiO₂-ZnO exhibits higher rate constants than that of unmodified TiO₂ and TiO₂-Ag-Zr for approximately 2.0 and 1.3 times, respectively. This is due to the strong activation to generate the reactive species under UV irradiation in both TiO₂ and ZnO

Table 2. The rate constants of MB degradation of the composite foams with various concentrations of TiO₂, TiO₂-ZnO and TiO₂-Ag-Zr under UV and fluorescent conditions.

TiO ₂ contents [phr]	Kinetic constant, $k \cdot 10^{-2}$ [h ⁻¹]					
	UV light			Fluorescent light		
	TiO ₂	TiO ₂ -ZnO	TiO ₂ -Ag-Zr	TiO ₂	TiO ₂ -ZnO	TiO ₂ -Ag-Zr
0	1.96	1.96	1.96	0.48	0.48	0.48
5	3.33	9.33	6.40	0.66	3.73	2.27
10	5.59	10.75	8.44	1.14	5.16	4.18
15	4.75	–	8.36	1.01	–	4.05
20	4.24	–	7.40	0.90	–	4.28

nanoparticles, leading to the move e_{cb}^- - and h_{vb}^+ of each semiconductor to others, resulting in the decrease of $e_{cb}^-h_{vb}^+$ pair recombination. For the case of TiO_2 -Ag-Zr, the e_{cb}^- in the valence band of TiO_2 is excited to the conduction band before transferring to the Ag nanoparticles, which act as the electron acceptor for enhancing the charge separation. However, in the case of unmodified TiO_2 , the lowest rate constant is observed when compared to the modified TiO_2 . This is attributed to the broad energy band gap that easily generates $e_{cb}^-h_{vb}^+$ recombination by reducing the reactive hydroxyl radicals to react with MB molecules. In addition, in the case of the measurement under the fluoresce condition, the modified TiO_2 exhibited a rate constant for degrading MB at approximately 4–5 times greater than the unmodified TiO_2 . It indicates that the visible region of unmodified TiO_2 does not have enough energy to support the excitation of charge carriers within the particle and causes a limitation of photocatalytic generation. Considering the results under the different light source conditions, the foam with modified TiO_2 under the UV light showed higher rate constants than the visible irradiation by approximately two times. It means that the higher energy of a photon in the UV region provides a greater degree of reactive radicals of OH^\bullet that is favorable for photocatalytic reaction. It corresponds to the faster degradation rate of MB by the composite relative to the one testing under fluorescent conditions. In the case of unmodified TiO_2 , the photocatalytic reaction is activated under UV light, but it shows an inactive behavior upon exposure under visible conditions. These results indicate that the composite foam filled with modified TiO_2 strongly extends the range of photocatalytic activity under UV and visible ranges.

To consider the performance of composite foam to degrade organic compounds in the gaseous phase, benzene gas degradation via the photocatalytic process is investigated under visible light by using a LED lamp as a light source. The composite foams filled with 10 phr of unmodified and modified TiO_2 showed the optimum MB degradation, and these foams were selected to assess benzene degradation at an initial concentration of 100 ppm. Figure 7a shows the adsorption and degradation of benzene gas by the foam through the photocatalytic process under visible light. Benzene gas is absorbed into the NR foam until it reaches an equilibrium adsorption state for approximately 4 h in darkness. The microporous

structure of the composite foam induces the intermolecular force of attraction between benzene and NR molecules through physisorption. Under visible light, the benzene gas concentration is found to be decreased continuously upon increasing the irradiation time, especially in the composite foam filled with modified TiO_2 . Although the foam filled with unmodified TiO_2 shows benzene adsorption, it has not performed photocatalytic action. It proves the occurrence of photocatalytic degradation reaction of modified TiO_2 . Excitation of e_{cb}^- in modified TiO_2 structure induces the generation of strong reactive OH^\bullet radicals that transfer to the bound rubber layer and degrades the benzene molecules. The possibilities of degrading benzene are through the reaction between OH^\bullet and benzene to generate phenol before producing 1,4-benzoquinone, hydroquinone, and catechol forms [47]. Also, the ring opening of phenol is the main reason for producing malonaldehyde form [48], as shown in the proposed model (Figure 7a). The improved photocatalytic activity to degrade benzene gas under visible light of modified TiO_2 can be attributed to the narrow energy band gap and also enhanced the charge transferring that corresponded to UV-visible absorption as already shown in Figure 3. It is also found that the use of TiO_2 -ZnO shows higher photocatalytic activity than TiO_2 -Ag-Zr. It is related to the kinetics of the degradation rate of the composites, as shown in Table 3. It can be seen that TiO_2 -ZnO has higher rate constants than the one with TiO_2 -Ag-Zr, approximately 2.0 times. This is attributed to the heterojunction form of TiO_2 and ZnO nanoparticles expected to lower the $e_{cb}^-h_{vb}^+$ recombination that enormously produced the reactive hydroxyl radicals to react with benzene molecules. The well gaseous adsorption of the composite foam is due to the open-cell structure that consists of small pores and large surface area to act as an adsorbent in the composites foam, as shown in the degree of dispersion of the elements inside the NR matrix based on the SEM-EDX analysis (Figure 7b). The result shows a slight change in the dispersion of elements inside the foam matrix. Unmodified and modified TiO_2 show uniform dispersion inside the foam. Furthermore, it is noted that Zn atoms are presented existed in all the specimens due to the presence of ZnO white seal as it has been used to activate the vulcanization process. The uniform dispersion of Ti elements in the foam filled with unmodified TiO_2 (Figure 7b) activates the photocatalytic process under UV

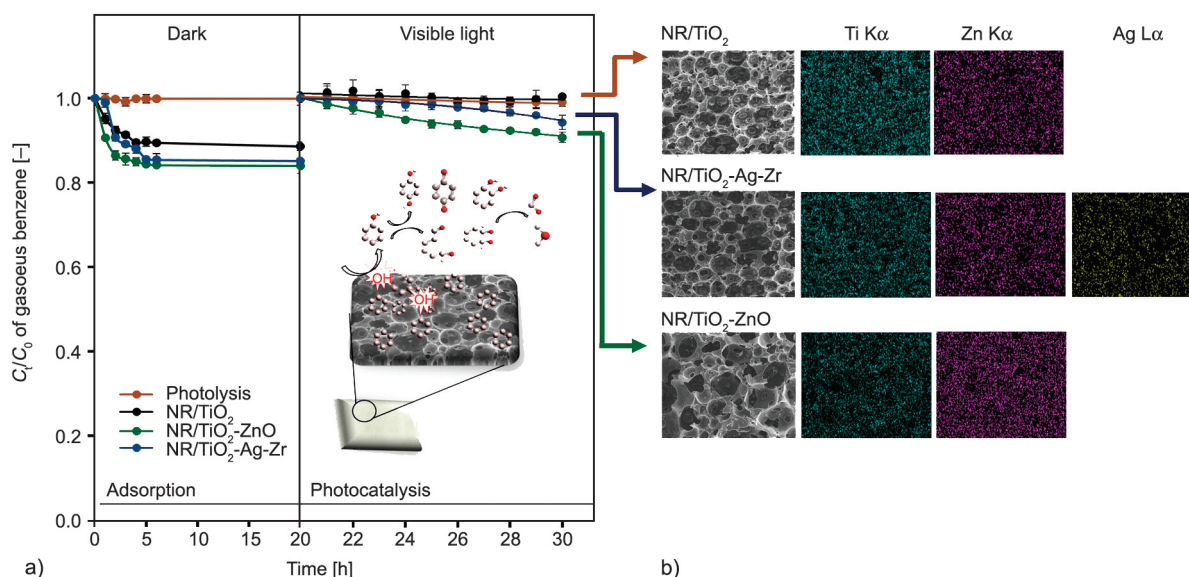


Figure 7. Adsorption and photocatalytic degradation of benzene gas by the composite foams under dark and visible irradiation conditions (a) and SEM-EDX images of the composite foams filled with 10 phr of TiO₂, TiO₂-ZnO, and TiO₂-Ag-Zr (b).

Table 3. Rate constants of benzene degradation of the composite foam under visible irradiation.

NR composite types	Kinetic constant, $k \cdot 10^{-2}$ [h ⁻¹]
NR/TiO ₂	0.02
NR/TiO ₂ -ZnO	0.99
NR/TiO ₂ -Ag-Zr	0.45

irradiation, but it is found to be inactive in visible irradiation as seen in the degradation of MB (Figure 5) and benzene molecules (Figure 7a). In the case of the composite foam filled with modified TiO₂, Ti and Ag elements can be seen in TiO₂-Ag-Zr particles, while strongly packed Zn atoms due to the deposition of ZnO nanoparticles on the TiO₂ surface are observed in the foam filled with TiO₂-ZnO. The uniform dispersion of modified TiO₂ in the foam generates $e_{cb}^- - h_{vb}^+$ pairs and charge transfers to the foam surface by enhancing the efficiency of degrading organic compounds in liquid and gaseous forms under both UV and visible conditions.

3.3. Mechanical properties of the composite foam

The reinforcement efficiency of unmodified and modified TiO₂ in the NR foam is determined based on the mechanical properties in terms of stress-strain diagram, modulus at 100% elongation, tensile strength, and elongation at break, as shown in Figure 8 and Table 4. From the stress-strain curves shown in Figure 8a, deformation resistance due to the filler-

reinforced NR matrix and the existence of strain-induced crystallization as indicated by the straight line of the plots [49]. The addition of all types of TiO₂ considerably increases the moduli at 100% elongation, Young's moduli, and tensile strengths of the foam. Also, the toughness of the foam estimated from the area under the stress-strain curve is increased upon filler reinforcement, whereas the elongation at break is decreased due to the hindering of NR molecular chain mobility based on bound rubber absorption onto the TiO₂ surface. The optimum value of tensile strength and estimated toughness are observed at 10 phr for TiO₂ and TiO₂-ZnO, while the optimum is observed at 15 phr in the case of TiO₂-Ag-Zr. Beyond these concentrations, tensile properties are significantly lowered due to the agglomeration of fillers inside the NR matrix, leading to poor filler-rubber interaction and reducing the filler reinforcement effect [50]. This region of agglomeration initiates the breaking point and is easy to break during extension, thus, the foam exhibits less deformation resistance, and the crack propagates rapidly. Among the foams of TiO₂ (Figure 10b and Table 4), there are no significant differences in 100% and Young's moduli of the composite foam, while the values of tensile strength, elongation at break and estimated toughness can be distinguished. As expected, the foam filled with TiO₂-Ag-Zr shows higher values of such properties compared to others. This is attributed to the small particle size with a high surface area for

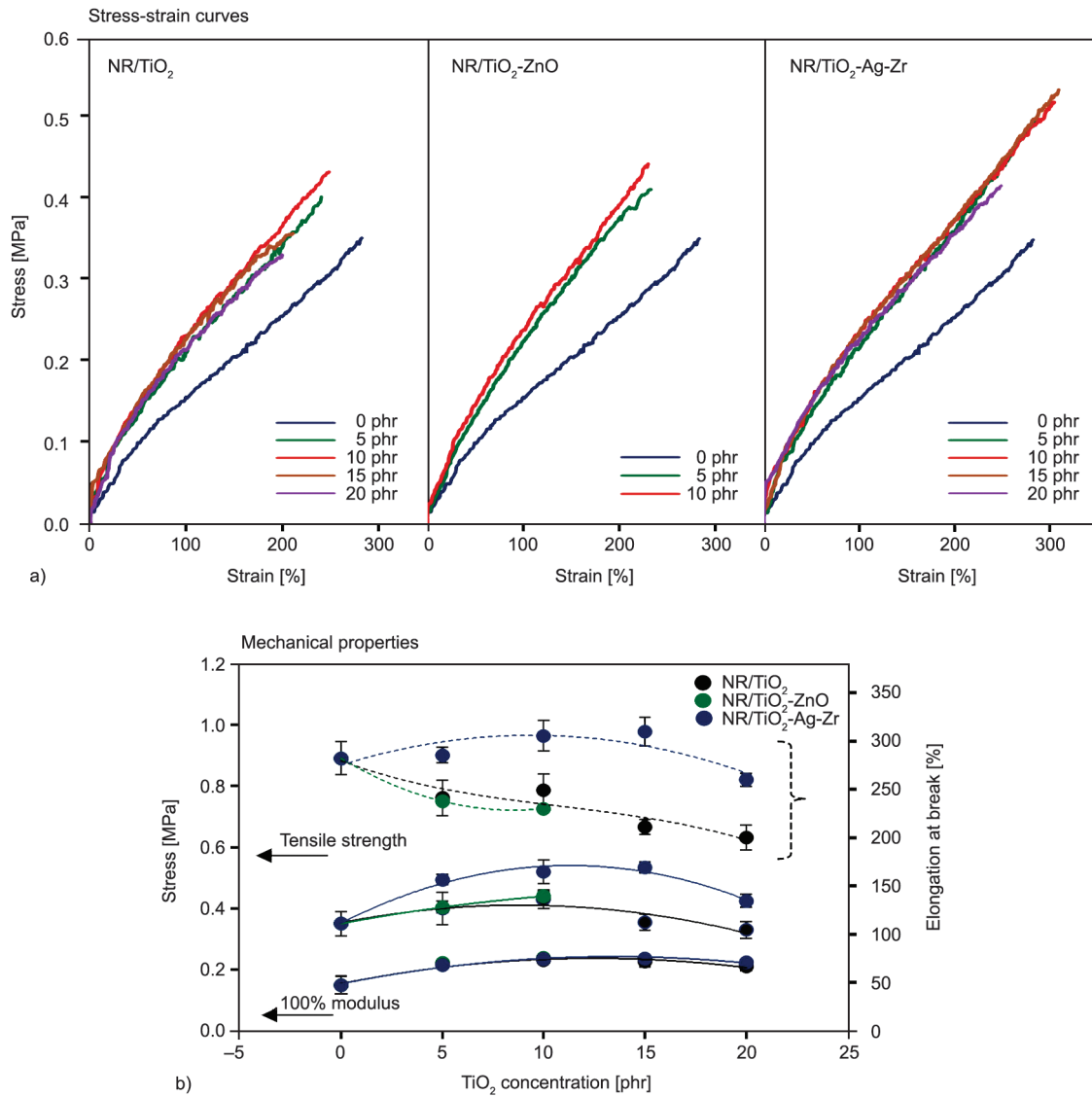


Figure 8. Stress-strain curves of the composite foams filled with TiO₂, TiO₂-ZnO, TiO₂-Ag-Zr (a) and the observed 100% modulus, tensile strength and elongation at break of the composite foams (b).

Table 4. Young’s modulus and toughness of the composite foams filled with TiO₂, TiO₂-ZnO, TiO₂-Ag-Zr.

TiO ₂ content [phr]	Young’s modulus [MPa]			Toughness [J/m ³]		
	TiO ₂	TiO ₂ -ZnO	TiO ₂ -Ag-Zr	TiO ₂	TiO ₂ -ZnO	TiO ₂ -Ag-Zr
0	0.0018	0.0018	0.0018	54.28	54.28	54.28
5	0.0024	0.0025	0.0024	55.41	55.49	78.58
10	0.0025	0.0026	0.0026	63.36	59.97	91.90
15	0.0023	N/A	0.0025	46.83	N/A	91.01
20	0.0023	N/A	0.0023	40.49	N/A	67.03

interacting with NR molecules of the filler, as shown in the TEM images (Figure 4). Therefore, the interaction between filler-rubber is effectively increased and resists the deformation of foam under stress. The reinforcement efficiency of three types of TiO₂ in NR composite foam can be explained by the arrangement of the NR molecular chain during

extension through the Mooney-Rivlin fitting with stress-strain behavior using Equation (4) [51]:

$$\sigma^*(\lambda) = \frac{\sigma(\lambda)}{\lambda - \lambda^{-2}} = 2(C_1 - C_2\lambda^{-2}) \quad (4)$$

where $\sigma^*(\lambda)$ is the reduced engineering stress, $\sigma(\lambda)$ is the engineering stress, C_1 and C_2 are the characteristic

constants of network chains determined from the intercept and the slope of the curves, respectively. The extension ratio λ is denoted as $\lambda = 1 + \varepsilon$, where ε is the engineering strain. The plots of reduced stress ($\sigma^*(\lambda)$) versus extension ratio ($1/\lambda$) of the composite foam filled with TiO_2 , $\text{TiO}_2\text{-ZnO}$, and $\text{TiO}_2\text{-Ag-Zr}$ with different loadings are shown in Figure 9. The chemical and physical interactions of the foam are elucidated from the observed values of C_1 as the Y-intercept and C_2 is obtained from the slope of the linear fit. Here, C_1 refers to the chemical interaction (*i.e.* crosslink density), and C_2 is related to the physical interaction (molecular chain entanglement, physical absorption) [52, 53]. According to the incorporation of TiO_2 , C_2 exhibited higher values than C_1 . It clarifies that most of the NR molecules well interact with the filler surface through physical chain entanglement based on their intermolecular chain attraction. The C_2 value is increased upon the addition of 10–15 phr of each TiO_2 loading. This correlates well with the increased 100% and Young’s moduli of the foam. It means that the proper addition of TiO_2 with better dispersion in the foam enhanced the reinforcement degree of filler to the rubber matrix. In Figure 9, it is clearly seen that the TiO_2 loading over 15 phr lowers the C_2 values due to the agglomeration of filler particles in the NR matrix. On comparing the composite foam with three types of TiO_2 , the C_2 values do not show a significant difference that is related to 100% and Young’s moduli as shown in Figure 8 and Table 4.

3.4. Antibacterial property of the composite foam

The antibacterial ability of the composite foams incorporated with TiO_2 , $\text{TiO}_2\text{-ZnO}$ and $\text{TiO}_2\text{-Ag-Zr}$ is investigated using *Escherichia coli* (*E. coli*) as a representative of gram-negative bacteria through the inhibition zone test, as shown in Figure 10. Also, the observed diameter of the clear zone is listed in Table 5. Here, the negative control sample is the foam without TiO_2 and ZnO particles and it clearly shows that there is no inhibition zone. Hence, the pure foam could not perform as antibacterial material. On the other hand, the inhibition zones are clearly demonstrated in cases of the composite foams filled with TiO_2 , $\text{TiO}_2\text{-ZnO}$ and $\text{TiO}_2\text{-Ag-Zr}$. It should be noted that the antibacterial properties of the foam with TiO_2 is attributed to the existence of ZnO (official ZnO grade, namely white seal ZnO). According to our previous work [54]. It is found that the ZnO has good antibacterial properties, which are directly related to its surface areas. This means that the use of ZnO nanoparticles in $\text{TiO}_2\text{-ZnO}$ and $\text{TiO}_2\text{-Ag-Zr}$ might provide superior bacterial killing ability under the controlled time. Thus, it is clearly seen in Figure 10 and Table 5 that the composite foam filled with unmodified TiO_2 showed a larger inhibition zone than the one with unfilled TiO_2 , but it exhibits much smaller zones than that of modified TiO_2 . In the case of $\text{TiO}_2\text{-ZnO}$, the antibacterial activity has taken place by creating reactive oxygen species

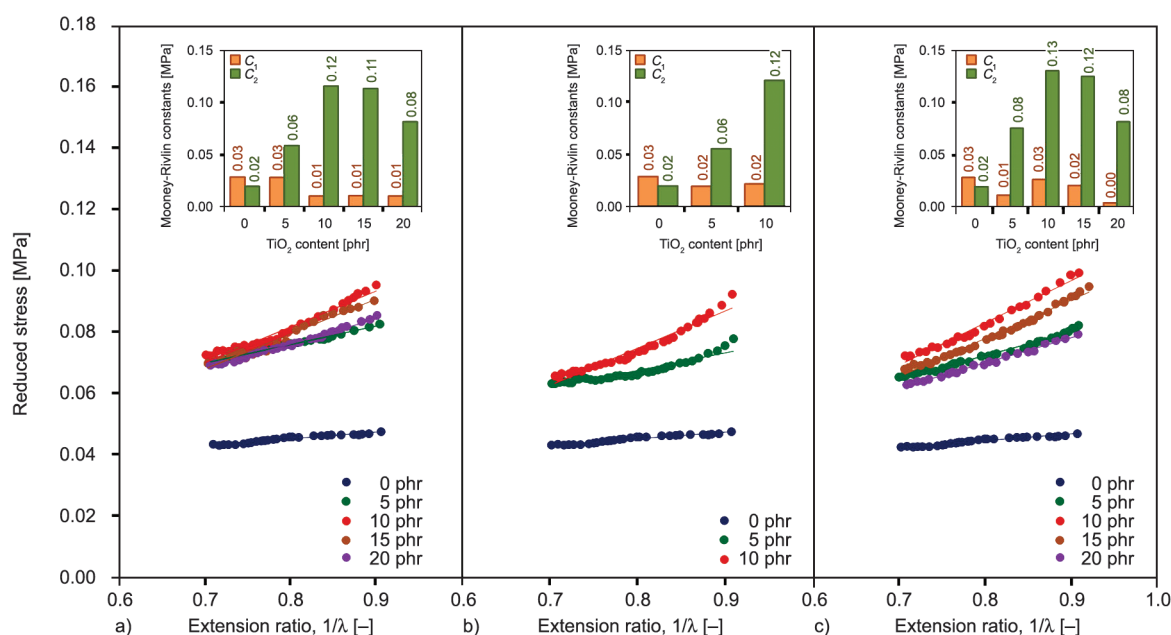


Figure 9. Reduced stress versus reciprocal extension ratio ($1/\lambda$) of the composite foams filled with TiO_2 (a), $\text{TiO}_2\text{-ZnO}$ (b), $\text{TiO}_2\text{-Ag-Zr}$ (c), in the inserted figures C_1 is the Y-intercept and C_2 is slope of the linear fit.

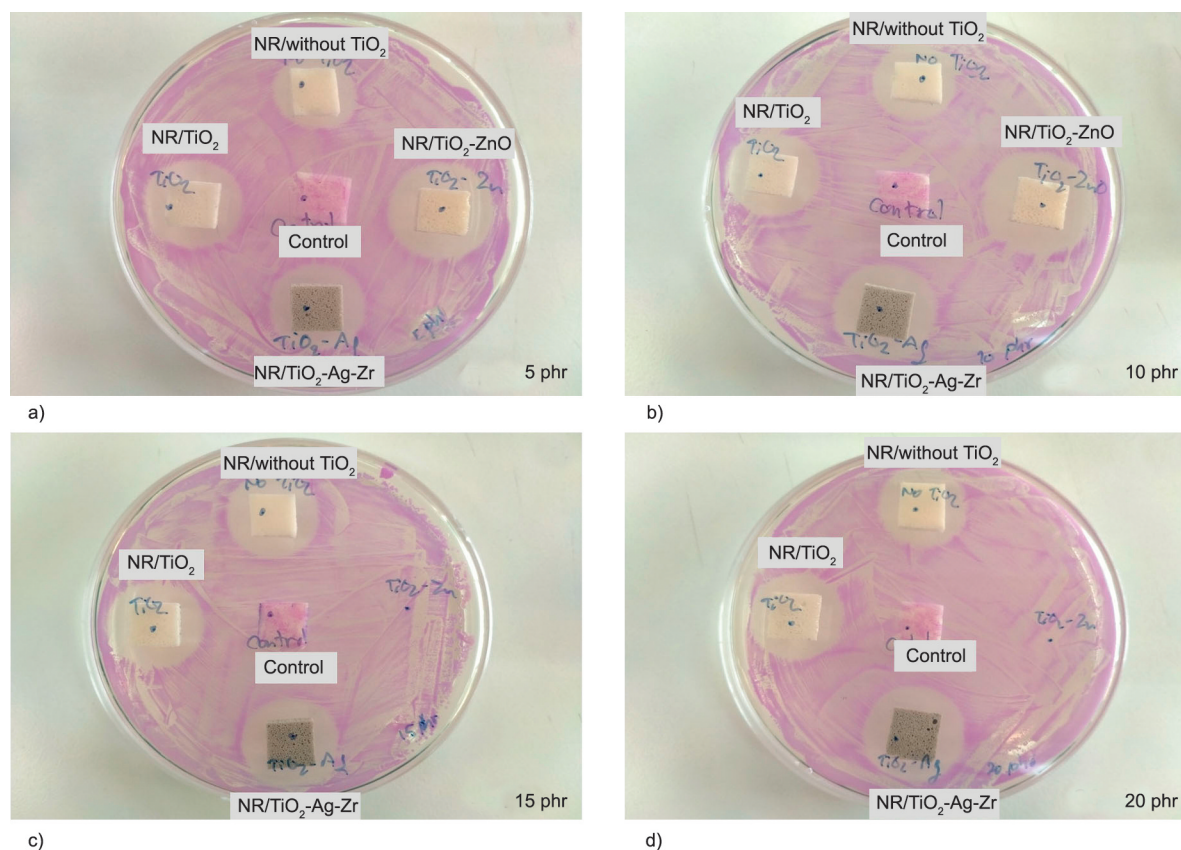


Figure 10. The qualitative antibacterial activity against gram-negative *E. coli* of the composite foam filled with TiO_2 , TiO_2 -ZnO and TiO_2 -Ag-Zr at loading at 5 phr (a), 10 phr (b), 15 phr (c) and 20 phr (d).

Table 5. Diameter of inhibition zone of the composite foam filled with TiO_2 , TiO_2 -ZnO, TiO_2 -Ag-Zr.

TiO ₂ content [phr]	Inhibition zone [cm]		
	TiO ₂	TiO ₂ -ZnO	TiO ₂ -Ag-Zr
0	1.75±0.10	1.75±0.10	1.75±0.10
5	1.80±0.11	2.10±0.10	1.85±0.05
10	1.85±0.05	2.25±0.16	1.95±0.09
15	1.85±0.09	–	1.90±0.08
20	1.85±0.05	–	1.95±0.05

(ROS) *i.e.* $\cdot\text{OH}$, $\cdot\text{OOH}$, $\cdot\text{O}_2^-$ and H_2O_2 , as well as the zinc(II) ions (Zn^{2+}) to disrupt the bacterial cell membrane [55]. The formation of ROS species on the filler surface is contributed to the photocatalytic reaction, as proposed in Figure 6a. Under the illumination of light, the e_{cb}^- , h_{vb}^+ pairs are originated based on the transition of e^- from the valence band to the conduction band. h_{vb}^+ in the valence band oxidizes moisture to form hydroxyl radical ($\cdot\text{OH}$), while e_{cb}^- in the conduction band reacts with the oxygen and creates superoxide radicals ($\cdot\text{O}_2^-$) before reacting with H^+ . Further, it forms peroxy radical ($\cdot\text{HOO}$) and hydrogen peroxide (H_2O_2), and finally reduces itself

to OH^* . Among the ROS species, $\cdot\text{OH}$ and H_2O_2 are able to penetrate the bacterial membrane [56], while the negative charges of $\cdot\text{O}_2^-$ do not penetrate through the strongly negative charges of the *E. coli* cell wall [57]. This means that the $\cdot\text{OH}$ plays an important role in the antibacterial properties of penetrating into the outer membrane, oxidizing membrane fatty acid, lipid, and protein, and also it damages the DNA [58]. Damage and penetration of intracellular components finally lead to cell death. Zn^{2+} ions are another important factor that effectively inactivated the bacteria. Here, the Zn^{2+} ions are penetrated into the cell membrane and disrupt DNA on the cellular of bacteria by inhibiting the transportation along with the amino acid metabolism and disturbing the enzyme system, also resulting in the bacteria cell death [59], as shown in the proposed model (Figure 11). It clearly explains the increased inhibition zone of the foam with various ZnO loadings. In the case of the foam filled with TiO_2 -Ag-Zr, the inhibition zone of the composite increases upon increasing TiO_2 -Ag-Zr to 10 phr. This results in the release of Ag ions (Ag^+) from Ag nanoparticles. The positive charges of Ag^+ ions have a strong electrostatic interaction with the

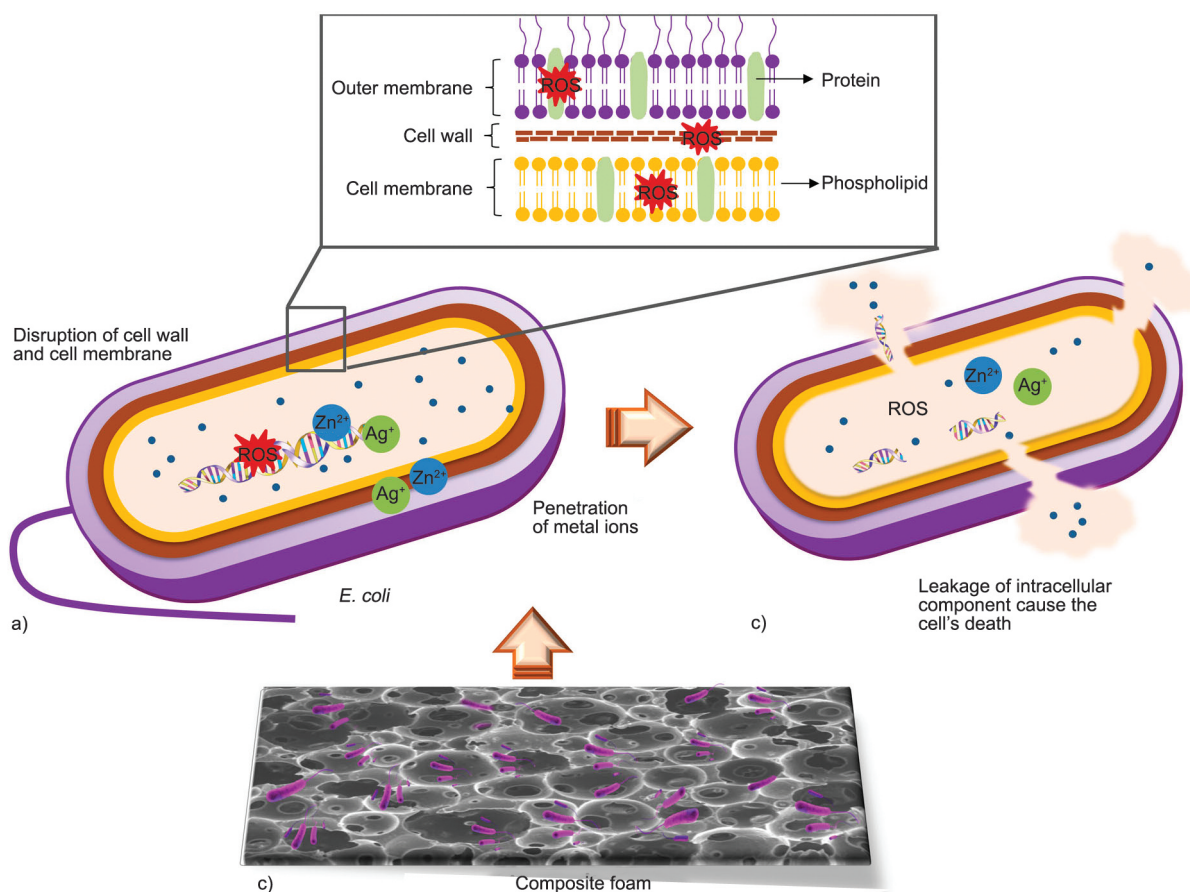


Figure 11. Proposed model of antibacterial mechanism of composite foam filled with modified TiO₂.

negative charges of the gram-negative bacterium *E. coli*. The Ag⁺ ions are penetrated into the cell wall and interact with the protein, lipid, DNA, and other biomolecules resulting in the leakage of cellular components and led to inhibit cell multiplication [60]. In addition, the excitation of e_{cb}^- in the Ag nanoparticles and transfer of its electron to Zr doped-TiO₂ induce the creation of ROS species from the photocatalytic reaction, as shown in the proposed model (Figure 6b). Such ROS damages the cell membrane and other components, leading to cell death. On comparing the types of modified TiO₂, the optimal concentration of TiO₂-ZnO and TiO₂-Ag-Zr to inhibit the growth of bacteria cells at 10 phr is comparable with the degradation of MB solution (Figure 5). The incorporation of TiO₂-ZnO shows the clear zone with large diameter than TiO₂-Ag-Zr, indicating the strong release of the produced ROS and Zn²⁺ against the *E. coli* growth. In addition, the amount of Zn²⁺ ions of TiO₂-ZnO is higher than Ag⁺ ions, as seen in the XPS spectra (Figure 2a), which exhibits higher antibacterial activity. Therefore, the generation of ROS species through photocatalytic and releasing of metal ions can move across the thin

rubber film by electrostatic force [54] that is sufficient for the degradation of the dye solution and destroy the bacterial cell membrane.

3.5. Air flowability through the complex composite foam structures

Since the incorporation of modified TiO₂ has strongly affected the intrinsic properties of NR foam in terms of dye degradation, gaseous benzene elimination, elastic properties, and antibacterial activity, in order to explain the foam structure, the air flowability is examined relative to other commercial foams, as seen in Table 6. It is seen that each foam shows significant differences in its behavior, but the developed composite foams showed lower air permeable values than the commercial foams. This is contributed by the complex rubber-foam structure, which retards the air movement through the material. Thus, the pollution trapping of the foam is consequently increased. Among the composites foams filled with unmodified and modified TiO₂, the foam with TiO₂-ZnO exhibited the lowest air permeability, which correlated well to the presented results based on benzene and bacteria trapping, removing, and

Table 6. Air permeability of composite foam filled with TiO₂, TiO₂-ZnO, and TiO₂-Ag-Zr comparative with the commercial masks.

Material types	Air permeability [l/min]
NR foam	30.1±1.8
NR/TiO ₂ foam	22.0±0.8
NR/TiO ₂ -ZnO foam	12.5±0.2
NR/TiO ₂ -Ag-Zr foam	15.7±0.3
Surgical mask	22.7±0.4
Fabric mask	77.0±2.0
PU foam	104.0±0.8

eliminating. As the received results, it is seen that the key factor for designing the specific composites foams properties is the intrinsic foam structures so that the engineering simulation of the air flowability is then considered.

From the high-resolution μ CT, the 2D images of the NR foams samples are converted to 3D object and the example is shown in Figure 12. With the simulation, the reconstructed object is used to determine the volume fraction of the sample by comparing the volume of material with the exterior volume. Therefore, the relative density (ρ^*) can be calculated by using Equation (5) where V_{foam} is the volume of the foam and V_{unit} is the volume of the cubic cell:

$$\rho^* = \frac{V_{\text{foam}}}{V_{\text{unit}}} \quad (5)$$

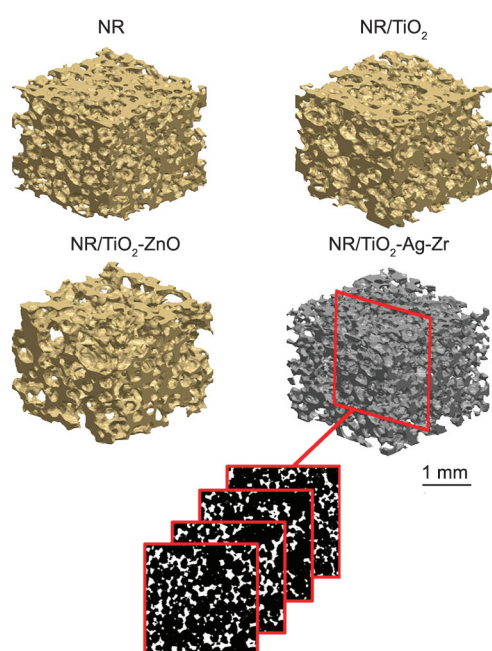


Figure 12 show the μ CT images and the ρ^* values of the NR composites foams with and without various TiO₂. It is clearly seen that the addition of unmodified TiO₂ does not change the relative density of the foam significantly. On the other hand, the incorporation of TiO₂-ZnO and TiO₂-Ag-Zr effectively decreases the ρ^* values by approximately 30%. It means that the addition of reinforcements with smaller particle sizes restricts the movement of NR molecular chains by increasing the physical interaction. This is well-known in the field of rubber as the bound rubber absorption (see in the inserted image of Figure 12). With this phenomenon, the porosity of the foam is found to be larger compared to the one without filler and with unmodified TiO₂, which do not reinforce much in the NR matrix. It correlates well with the tensile properties, VOC absorption and antibacterial ability of the composite foam that increases by minimizing the size of TiO₂ particles. However, although the ρ^* values of NR/TiO₂-ZnO and NR/TiO₂-Ag-Zr exhibited no significant differences, the void morphologies of both the composite foams are noticeably different. It is seen that the NR/TiO₂-ZnO exhibited a larger pore size than those of NR/TiO₂-Ag-Zr. Thus, it is expected that, the fluid permeabilities of both structures are unidentical. Based on the μ CT images, the geometrical architectures of porous materials are simulated from the computational fluid dynamics (CFD) by relating the

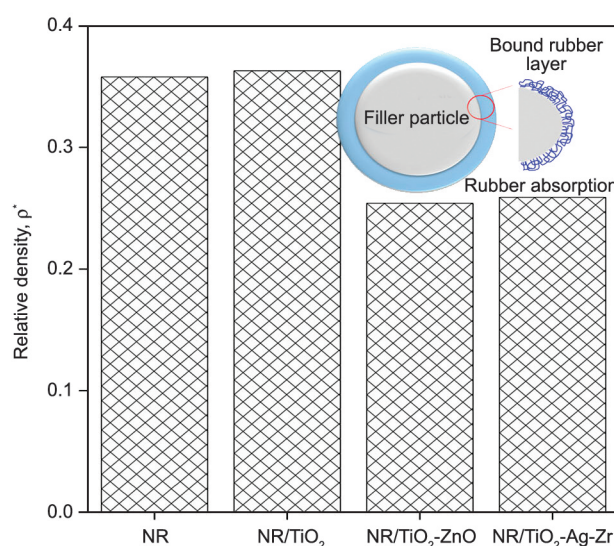


Figure 12. The 3D geometries and relative densities of composite foam filled with modified TiO₂.

effect of morphologies on the flow [61, 62]. It is known that the CFD analysis enables the simulation of fluid flowing through the foams. It is closely related to observing the influence of foam architectures on flow behaviors. To obtain the flow behavior numerically, the Navier-Stokes equation formulated based on the conservation of mass and momentum as shown in Equations (5) and (6), needs to be solved via computational evaluation. In addition, Figure 13a illustrates the CFD computational domain, which consists of the air channel and composite foams. When the air flows along the y-axis, the driving force from the pressure difference is imposed at both ends of the flow domain. Thus, it can be seen that the foam size of 2 mm is smaller than the actual foam used in experiments. The reasons for small domains adopted in the CFD analysis are as follows,

- (i) Rubber foam, as seen in Figure 13a exhibits a few features. Thus, the large foam for CFD analysis is strictly limited by the available computational resources.
- (ii) A small foam domain could be considered as the representative volume element (RVE) domain, which is assumed to represent the behavior of larger foam.

A similar idea has been adopted by the material science community when microstructural features noticeably impact the physical behavior at the macro-level [63]. Once the simulated flow fields are obtained, the fluid permeability (k) can be calculated using Darcy’s law, as shown in Equation (7) [64]. Based on Equation (7), the samples with higher permeability imply greater mass transport through the structures (Equations (6)–(8)):

$$\rho \frac{\partial \vec{u}}{\partial t} - \mu \nabla^2 \vec{u} + \rho (\vec{u} \cdot \nabla) \vec{u} + \nabla p = 0, \quad \nabla \cdot \vec{u} = 0 \quad (6)$$

$$\nabla = \frac{\partial}{\partial x} i + \frac{\partial}{\partial y} j + \frac{\partial}{\partial z} k \quad (7)$$

$$k = \frac{Q\mu L}{A\Delta p} \quad (8)$$

where A is the cross-sectional area of a fluid domain, L and p are the unit cell size and pressure, Q and t refer to the flow rate and time consumption. Also, \vec{u} and μ are the velocity vector and dynamic viscosity, ∇ is the partial derivative, x, y, z are the spatial coordinates, ρ and ρ^* are the density and relative density, respectively.

Thus, corresponding to the CFD simulation and calculation of Equations (6) and (7), the simulated flow

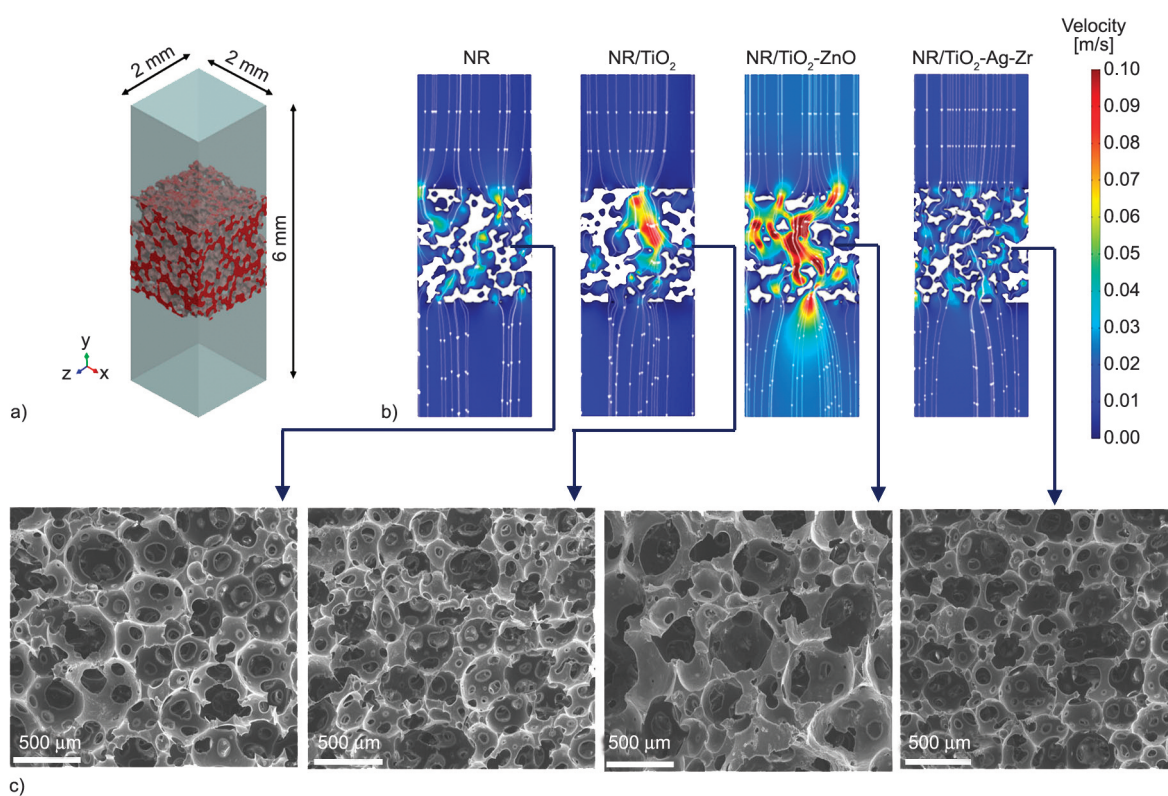


Figure 13. 3D structural scanning (a) and simulated flow profiles sectioned along the mid-plane of 3D models (b) and SEM images of the composite foams (c) filled with modified TiO₂.

profiles are sectioned along the mid-plane of 3D models, as shown in Figure 13b. It is clearly seen that the air flowing through each composite foam is established relating to the air velocity. It is found that the air flow has not entirely related to the calculated ρ^* values. This is due to the porous nature of NR foam as it has not only formed circular shapes of the closed-cell, but it is opened-cell foam with connected porous regions. It means that the value of ρ^* of the foam does not have difficulty in air flowing. With the complex structures, NR and NR/TiO₂-Ag-Zr composite foams exhibited poor air flow, whereas smooth air flow is observed in the NR composite foam with TiO₂-ZnO even though the same pressure is applied. This correlates well with the morphologies of the composite foams, as seen in Figure 13c. NR/TiO₂-ZnO foam showed larger opened cells that are well connected with each other. It clearly supports the highest gaseous benzene elimination and absorption together with antibacterial properties of the composite foam, as seen in Figure 7 and 10, respectively. According to the simulated flow profiles, Darcian permeabilities are calculated based on both experiments and numerical simulation, as seen in Table 7 by using Equation (8) and compared with the predicted Darcian permeabilities by Poltue *et al.* [61]. The authors performed a numerical prediction of

permeabilities for six different porous structures. Results were clearly shown the dependency on both relative density and interconnect structures. Figure 14 showed the upper and lower bounds of Darcian permeabilities from Poltue *et al.* [61]. Also, the results from the present work are mapped and compared. It is noted that Figure 14 shows a noticeable deviation between experiments and numerical results, which can be attributed to various factors, such as stochasticity aspects of the different foams, geometrical deviation from the resolution of μ CT, or deviation contributed from the 3D reconstruction process. Approximately a difference of 1 order of magnitude in the k values is observed upon comparing the results based on experimental ($k_{\text{exp.}}$) and prediction ($k_{\text{pred.}}$). This is generally related to the unidentified porous shapes of NR foam and, therefore, the values of $k_{\text{pred.}}$ is found to be lowered, and it is assumed that all the pores have spherical shapes. In addition, the trend of k is slightly changed since the $k_{\text{exp.}}$ of NR/TiO₂-ZnO and NR/TiO₂-Ag-Zr are slightly lower than the NR and NR/TiO₂ foams. Also, it is clearly seen that the $k_{\text{exp.}}$ of the composite foams with modified TiO₂ are out of the prediction of Poltue *et al.* [61] (see as the light-red area in Figure 14). As expected, it is related to the complex porous structures of NR foam after the addition of the reinforcing filler. It is well suggested that the flow ability and breathability are primarily controlled by the thickness of foams. With this foam designing, it tends to lower the bound and the structural stochasticity of foam exhibits adverse effects on fluid permeabilities, which can be applied in the manufacturing of filtered masks.

Table 7. Darcian permeability of different foams obtained from experiment and numerical modeling.

Samples	Experimental k , $k_{\text{exp.}}$ [m ²]	Predicted k , $k_{\text{pred.}}$ [m ²]
NR	$5.43 \cdot 10^{-11}$	$1.12 \cdot 10^{-10}$
NR/TiO ₂	$3.80 \cdot 10^{-11}$	$1.11 \cdot 10^{-10}$
NR/TiO ₂ -ZnO	$3.30 \cdot 10^{-11}$	$2.54 \cdot 10^{-10}$
NR/TiO ₂ -Ag-Zr	$2.27 \cdot 10^{-11}$	$1.70 \cdot 10^{-10}$

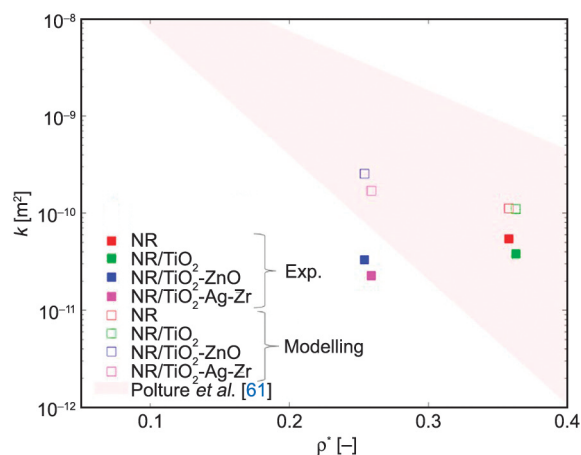


Figure 14. Darcian permeability from experiment and numerical modeling based on Equation (8).

4. Conclusions

NR composite foams filled with unmodified and modified TiO₂ with ZnO nanoparticle and Ag-Zr doping were carefully prepared following the latex processes in order to investigate the possibility of the foam for use as the filter application. Photocatalytic activity of the foam was controlled by the types and contents of the additional fillers. The results showed that the foam with modified TiO₂ lowered the band gap energy from 3.10 to 2.85–2.90 eV for the cases of TiO₂-ZnO and TiO₂-Ag-Zr. This allows photocatalytic propagation of the foam under both UV and visible lights. This also effectively causes the absorption of gaseous benzene due to the large production of reactive radicals to eliminate the organic substance. The mechanical properties of the foams

showed optimal Young's modulus, tensile strength, and toughness at 10 phr TiO₂ and TiO₂-ZnO and at 15 phr TiO₂-Ag-Zr. Significant reduction in tensile properties was observed when filler contents had increased owing to filler agglomeration. Along with solvent absorption, the inhibition of the foam against the gram-negative E.coli was investigated. It was found that the NR composite foams with both TiO₂-ZnO and TiO₂-Ag-Zr exhibited a clear inhibition zone due to the killing of bacteria based on the formation of ROS radicals together with and releasing of metal ions of Zn²⁺ or Ag⁺ to disrupt the bacterial cell structure. Thus, with the unique properties of foam, the air permeability with a proposed thickness of the foam was examined through engineering simulation. The porous size and shapes were simulated, and the *k* value was evaluated relating to other cubic cell which had fixed pore sizes and shapes. The evaluation represented that the foam had the ability to filtrate and can be categorized as low-bounds opened-cell foam. Therefore, the proposed NR composite foam showed suitable properties for applying as the filter application with unique properties of gaseous benzene elimination and absorption and antibacterial properties. It provides a new platform for using NR foam, which can be aimed for several filter applications, particularly for the petrol station, construction, oil refinery and other protective zones.

Acknowledgements

The authors gratefully acknowledge the financial support from the Post-doctoral Fellowship, King Mongkut's University of Technology Thonburi (KMUTT). Also, the support from the Program Management Unit for Human Resources & Institutional Development, Research and Innovation [grant number B01F630003] is acknowledged for the grant support.

References

- [1] Dallinga J. W., Robroeks C. M. H. H. T., van Berkel J. J. B. N., Moonen E. J. C., Godschalk R. W. L., Jöbsis Q., Dompeling E., Wouters E. F. M., van Schooten F. J.: Volatile organic compounds in exhaled breath as a diagnostic tool for asthma in children. *Clinical and Experimental Allergy*, **40**, 68–76 (2010).
<https://doi.org/10.1111/j.1365-2222.2009.03343.x>
- [2] Burchacka E., Pstrowska K., Beran E., Fałtynowicz H., Chojnacka K., Kulażyński M.: Antibacterial agents adsorbed on active carbon: A new approach for *S. aureus* and *E. coli* pathogen elimination. *Pathogens*, **10**, 1066 (2021).
<https://doi.org/10.3390/pathogens10081066>
- [3] Prasert A., Sontikaew S., Sriprapai D., Chuangchote S.: Polypropylene/ZnO nanocomposites: Mechanical properties, photocatalytic dye degradation, and antibacterial property. *Materials*, **13**, 914 (2020).
<https://doi.org/10.3390/ma13040914>
- [4] McEvoy J. G., Zhang Z.: Antimicrobial and photocatalytic disinfection mechanisms in silver-modified photocatalysts under dark and light conditions. *Journal of Photochemistry and Photobiology C: Photochemistry Reviews*, **19**, 62–75 (2014).
<https://doi.org/10.1016/j.jphotochemrev.2014.01.001>
- [5] Liu G., Huang H., Xie R., Feng Q., Fang R., Shu Y., Zhan Y., Ye X., Zhong C.: Enhanced degradation of gaseous benzene by a Fenton reaction. *RSC Advances*, **7**, 71–76 (2017).
<https://doi.org/10.1039/C6RA26016K>
- [6] Enesca A., Cazan C.: Volatile organic compounds (VOCs) removal from indoor air by heterostructures/composites/doped photocatalysts: A mini-review. *Nanomaterials*, **10**, 1965 (2020).
<https://doi.org/10.3390/nano10101965>
- [7] Rekhate C. V., Srivastava J. K.: Recent advances in ozone-based advanced oxidation processes for treatment of wastewater- A review. *Chemical Engineering Journal Advances*, **3**, 100031 (2020).
<https://doi.org/10.1016/j.cej.2020.100031>
- [8] He F., Jeon W., Choi W.: Photocatalytic air purification mimicking the self-cleaning process of the atmosphere. *Nature Communications*, **12**, 2528 (2021).
<https://doi.org/10.1038/s41467-021-22839-0>
- [9] Fujishima A., Rao T. N., Tryk D. A.: Titanium dioxide photocatalysis. *Journal of Photochemistry and Photobiology C: Photochemistry Reviews*, **1**, 1–21 (2000).
[https://doi.org/10.1016/S1389-5567\(00\)00002-2](https://doi.org/10.1016/S1389-5567(00)00002-2)
- [10] Ong C. B., Ng L. Y., Mohammad A. W.: A review of ZnO nanoparticles as solar photocatalysts: Synthesis, mechanisms and applications. *Renewable and Sustainable Energy Reviews*, **81**, 536–551 (2018).
<https://doi.org/10.1016/j.rser.2017.08.020>
- [11] Haspulat B., Saribel M., Kaniş H.: Surfactant assisted hydrothermal synthesis of SnO nanoparticles with enhanced photocatalytic activity. *Arabian Journal of Chemistry*, **13**, 96–108 (2020).
<https://doi.org/10.1016/j.arabjc.2017.02.004>
- [12] Dong P., Hou G., Xi X., Shao R., Dong F.: WO₃-based photocatalysts: Morphology control, activity enhancement and multifunctional applications. *Environmental Science: Nano*, **4**, 539–557 (2017).
<https://doi.org/10.1039/C6EN00478D>
- [13] Zhang T., Liu J., Zhou F., Zhou S., Wu J., Chen D., Xu Q., Lu J.: Polymer-coated Fe₂O₃ nanoparticles for photocatalytic degradation of organic materials and antibiotics in water. *ACS Applied Nano Materials*, **3**, 9200–9208 (2020).
<https://doi.org/10.1021/acsanm.0c01829>

- [14] Hoffmann M. R., Martin S. T., Choi W., Bahnemann D. W.: Environmental applications of semiconductor photocatalysis. *Chemical Reviews*, **95**, 69–96 (1995).
<https://doi.org/10.1021/cr00033a004>
- [15] Sucher N. J., Carles M. C., Nowotny J., Bak T.: Photocatalytic water disinfection on oxide semiconductors: Part 2 – Structure, functional properties and reactivity of microbial agents. *Advances in Applied Ceramics*, **111**, 16–33 (2012).
<https://doi.org/10.1179/1743676111Y.0000000039>
- [16] Siwińska-Stefańska K., Kubiak A., Piasecki A., Goscińska J., Nowaczyk G., Jurga S., Jesionowski T.: TiO₂-ZnO binary oxide systems: Comprehensive characterization and tests of photocatalytic activity. *Materials*, **11**, 841 (2018).
<https://doi.org/10.3390/ma11050841>
- [17] Banerjee A., Hamnabard N., Joo S.: A comparative study of the effect of Pd-doping on the structural, optical, and photocatalytic properties of sol-gel derived anatase TiO₂ nanoparticles. *Ceramics International*, **42**, 12010–12026 (2016).
<https://doi.org/10.1016/j.ceramint.2016.04.128>
- [18] Basavarajappa P. S., Patil S. B., Ganganagappa N., Reddy K. R., Raghu A. V., Reddy C. V.: Recent progress in metal-doped TiO₂, non-metal doped/codoped TiO₂ and TiO₂ nanostructured hybrids for enhanced photocatalysis. *International Journal of Hydrogen Energy*, **45**, 7764–7778 (2020).
<https://doi.org/10.1016/j.ijhydene.2019.07.241>
- [19] Sanitnon P., Chiarakorn S., Chawengkijwanich C., Chuangchote S., Pongprayoon T.: Synergistic effects of zirconium and silver *co*-dopants in TiO₂ nanoparticles for photocatalytic degradation of an organic dye and antibacterial activity. *Journal of the Australian Ceramic Society*, **56**, 579–590 (2020).
<https://doi.org/10.1007/s41779-019-00368-w>
- [20] Narkbuakaew T., Sujaridworakun P.: Role of Ag⁽⁰⁾ deposited on TiO₂ nanoparticles for superior photocatalytic performance induced by calcination. *Optical Materials*, **98**, 109407 (2019).
<https://doi.org/10.1016/j.optmat.2019.109407>
- [21] Habibi M. H., Talebian N., Choi J-H.: The effect of annealing on photocatalytic properties of nanostructured titanium dioxide thin films. *Dyes and Pigments*, **73**, 103–110 (2007).
<https://doi.org/10.1016/j.dyepig.2005.10.016>
- [22] Sriwong C., Choojun K., Sriwong S.: High photocatalytic performance of 3D porous-structured TiO₂@natural rubber hybrid sheet on the removal of indigo carmine dye in water. *SN Applied Sciences*, **1**, 864 (2019).
<https://doi.org/10.1007/s42452-019-0900-y>
- [23] Lin G., Tian M., Lu Y-L., Zhang X-J., Zhang L-Q.: Morphology, antimicrobial and mechanical properties of nano-TiO₂/rubber composites prepared by direct blending. *Polymer Journal*, **38**, 498–502 (2006).
<https://doi.org/10.1295/polymj.38.498>
- [24] Toh-ae P., Paradee N., Saramolee P., Chiarakorn S., Kalkornsurapranee E., Johns J., Nakaramontri Y.: Nanotitania doped NR foams: Influence on photocatalysis and physical properties. *Polymer Degradation and Stability*, **190**, 109640 (2021).
<https://doi.org/10.1016/j.polymdegradstab.2021.109640>
- [25] Zhan Y., Hao S., Li Y., Santillo C., Zhang C., Sorrentino L., Lavorgna M., Xia H., Chen Z.: High sensitivity of multi-sensing materials based on reduced graphene oxide and natural rubber: The synergy between filler segregation and macro-porous morphology. *Composites Science and Technology*, **205**, 108689 (2021).
<https://doi.org/10.1016/j.compscitech.2021.108689>
- [26] Xie Z., Cai Y., Zhan Y., Meng Y., Li Y., Xie Q., Xia H.: Thermal insulating rubber foams embedded with segregated carbon nanotube networks for electromagnetic shielding applications. *Chemical Engineering Journal*, **435**, 135118 (2022).
<https://doi.org/10.1016/j.cej.2022.135118>
- [27] Jang J., Hur H-G., Sadowsky M. J., Byappanahalli M. N., Yan T., Ishii S.: Environmental *Escherichia coli*: Ecology and public health implications – A review. *Journal of Applied Microbiology*, **123**, 570-581 (2017).
<https://doi.org/10.1111/jam.13468>
- [28] Bodilsen J., Brouwer M. C., Kjargaard N., Sirks M. J., van der Ende A., Nielsen H., van de Beek D.: Community-acquired meningitis in adults caused by *Escherichia coli* in Denmark and The Netherlands. *Journal of Infection*, **77**, 25–29 (2018).
<https://doi.org/10.1016/j.jinf.2018.05.009>
- [29] Sirivallop A., Areerob T., Chiarakorn T.: Enhanced visible light photocatalytic activity of N and Ag doped and *co*-doped TiO₂ synthesized by using an *in-situ* solvothermal method for gas phase ammonia removal. *Catalysts*, **10**, 251 (2020).
<https://doi.org/10.3390/catal10020251>
- [30] Rathnayake W. G. I. U., Ismail H., Baharin A., Bandara I., Rajapakse S.: Enhancement of the antibacterial activity of natural rubber latex foam by the incorporation of zinc oxide nanoparticles. *Journal of Applied Polymer Science*, **131**, 39601 (2014).
<https://doi.org/10.1002/app.39601>
- [31] Sombatmai A., Uthaisangsuk V., Wongwises S., Promopattum P.: Multiscale investigation of the influence of geometrical imperfections, porosity, and size-dependent features on mechanical behavior of additively manufactured Ti-6Al-4V lattice struts. *Materials and Design*, **209**, 109985 (2021).
<https://doi.org/10.1016/j.matdes.2021.109985>
- [32] Choo H., Sham K-L., Bohling J., Ngo A., Xiao X., Ren Y., Depond P. J., Matthews M. J., Garlea E.: Effect of laser power on defect, texture, and microstructure of a laser powder bed fusion processed 316L stainless steel. *Materials and Design*, **164**, 107534 (2019).
<https://doi.org/10.1016/j.matdes.2018.12.006>

- [33] Kim C., Choi H., Kim J. I., Lee S., Kim J., Lee W., Hwang T., Kang S., Moon T., Park B.: Improving scattering layer through mixture of nanoporous spheres and nanoparticles in ZnO-based dye-sensitized solar cells. *Nanoscale Research Letters*, **9**, 295 (2014).
<https://doi.org/10.1186/1556-276X-9-295>
- [34] Peerakiatkhajorn P., Chawengkijwanich C., Onreabroy W., Chiarakorn S.: Novel photocatalytic Ag/TiO₂ thin film on polyvinyl chloride for gaseous BTEX treatment. *Materials Science Forum*, **712**, 133–145 (2012).
<https://doi.org/10.4028/www.scientific.net/MSF.712.133>
- [35] Xiong L-B., Li J-L., Yang B., Yu Y.: Ti³⁺ in the surface of titanium dioxide: Generation, properties and photocatalytic application. *Journal of Nanomaterials*, **2012**, 831524 (2011).
<https://doi.org/10.1155/2012/831524>
- [36] Singh I., Kumar R., Birajdar B. I.: Zirconium doped TiO₂ nano-powder *via* halide free non-aqueous solvent controlled sol-gel route. *Journal of Environmental Chemical Engineering*, **5**, 2955–2963 (2017).
<https://doi.org/10.1016/j.jece.2017.05.046>
- [37] Suwanchawalit C., Wongnawa S., Sriprang P., Meanha P.: Enhancement of the photocatalytic performance of Ag-modified TiO₂ photocatalyst under visible light. *Ceramics International*, **38**, 5201–5207 (2012).
<https://doi.org/10.1016/j.ceramint.2012.03.027>
- [38] Makuła P., Pacia M., Macyk W.: How to correctly determine the band gap energy of modified semiconductor photocatalysts based on UV–vis spectra. *Journal of Physical Chemistry Letters*, **9**, 6814–6817 (2018).
<https://doi.org/10.1021/acs.jpcl.8b02892>
- [39] Pasche A., Grohe B., Mittler S., Charpentier P. A.: Zr-doped TiO₂ nanoparticles synthesized *via* a sol–gel route and their application in dye-sensitized solar cells for thermo-stabilization. *Materials Research Express*, **4**, 065501 (2017).
<https://doi.org/10.1088/2053-1591/aa742d>
- [40] Chen L-L., Zhai B-G., Huang Y. M.: Rendering visible-light photocatalytic activity to undoped ZnO *via* intrinsic defects engineering. *Catalysts*, **10**, 1163 (2020).
<https://doi.org/10.3390/catal10101163>
- [41] Bai N., Liu X., Li Z., Ke X., Zhang K., Wu Q.: High-efficiency TiO₂/ZnO nanocomposites photocatalysts by sol–gel and hydrothermal methods. *Journal of Sol-Gel Science and Technology*, **99**, 92–100 (2012).
<https://doi.org/10.1007/s10971-021-05552-8>
- [42] Ali T., Ahmed A., Alam U., Uddin I., Tripathi P., Muneer M.: Enhanced photocatalytic and antibacterial activities of Ag-doped TiO₂ nanoparticles under visible light. *Materials Chemistry and Physics*, **212**, 325–335 (2018).
<https://doi.org/10.1016/j.matchemphys.2018.03.052>
- [43] Chakhtouna H., Benzeid H., Zari N., el kacem Qaiss A., Bouhfid R.: Recent progress on Ag/TiO₂ photocatalysts: Photocatalytic and bactericidal behaviors. *Environmental Science and Pollution Research*, **28**, 44638–44666 (2021).
<https://doi.org/10.1007/s11356-021-14996-y>
- [44] Matsunami D., Yamanaka K., Mizoguchi T., Kojima K.: Comparison of photodegradation of methylene blue using various TiO₂ films and WO₃ powders under ultraviolet and visible-light irradiation. *Journal of Photochemistry and Photobiology A: Chemistry*, **369**, 106–114 (2019).
<https://doi.org/10.1016/j.jphotochem.2018.10.020>
- [45] Bellè U., Pelizzari F., Lucotti A., Castiglioni C., Ormellese M., Pedferri M., Diamanti M. V.: Immobilized nano-TiO₂ photocatalysts for the degradation of three organic dyes in single and multi-dye solutions. *Coatings*, **10**, 919 (2020).
<https://doi.org/10.3390/coatings10100919>
- [46] Tongon W., Chawengkijwanich C., Chiarakorn S.: Multifunctional Ag/TiO₂/MCM-41 nanocomposite film applied for indoor air treatment. *Building and Environment*, **82**, 481–489 (2014).
<https://doi.org/10.1016/j.buildenv.2014.09.014>
- [47] Park H., Choi W.: Photocatalytic conversion of benzene to phenol using modified TiO₂ and polyoxometalates. *Catalysis Today*, **101**, 291–297 (2005).
<https://doi.org/10.1016/j.cattod.2005.03.014>
- [48] Bui T. D., Kimura A., Higashida S., Ikeda S., Matsumura M.: Two routes for mineralizing benzene by TiO₂-photocatalyzed reaction. *Applied Catalysis B: Environmental*, **107**, 119–127 (2011).
<https://doi.org/10.1016/j.apcatb.2011.07.004>
- [49] Brüning K., Schneider K., Roth S. V., Heinrich G.: Kinetics of strain-induced crystallization in natural rubber studied by WAXD: Dynamic and impact tensile experiments. *Macromolecules*, **45**, 7914–7919 (2012).
<https://doi.org/10.1021/ma3011476>
- [50] Phomrak S., Nimpaiboon A., Newby B-Z., Phisalaphong M.: Natural rubber latex foam reinforced with micro- and nanofibrillated cellulose *via* dunlop method. *Polymers*, **12**, 1959 (2020).
<https://doi.org/10.3390/polym12091959>
- [51] Rivlin R. S., Saunders D. W.: Large elastic deformations of isotropic materials VII. Experiments on the deformation of rubber. *Philosophical Transactions of the Royal Society of London A*, **243**, 251–288 (1951).
<https://doi.org/10.1098/rsta.1951.0004>
- [52] Schlögl S., Trutschel M-L., Chassé W., Riess G., Saalwächter K.: Entanglement effects in elastomers: Macroscopic vs microscopic properties. *Macromolecules*, **47**, 2759–2773 (2014).
<https://doi.org/10.1021/ma4026064>
- [53] Saleesung T., Reichert D., Saalwächter K., Sirisinha C.: Correlation of crosslink densities using solid state NMR and conventional techniques in peroxide-crosslinked EPDM rubber. *Polymer*, **56**, 309–317 (2015).
<https://doi.org/10.1016/j.polymer.2014.10.057>

- [54] Krainoi A., Poomputsa K., Kalkornsuraanee E., Johns J., Songtipya L., Nip R., Nakaramontri Y.: Disinfectant natural rubber films filled with modified zinc oxide nanoparticles: Synergetic effect of mechanical and antibacterial properties. *Express Polymer Letters*, **15**, 1081–1100 (2021).
<https://doi.org/10.3144/expresspolymlett.2021.87>
- [55] Zhang L., Jiang Y., Ding Y., Daskalakis N., Jeuken L., Povey M., O'Neill A. J., York D. W.: Mechanistic investigation into antibacterial behaviour of suspensions of ZnO nanoparticles against *E. coli*. *Journal of Nanoparticle Research*, **12**, 1625–1636 (2010).
<https://doi.org/10.1007/s11051-009-9711-1>
- [56] Lakshmeesha T. R., Sateesh M. K., Prasad B. D., Sharma S. C., Kavyashree D., Chandrasekhar M., Nagabhushana H.: Reactivity of crystalline ZnO superstructures against fungi and bacterial pathogens: Synthesized using nerium oleander leaf extract. *Crystal Growth and Design*, **14**, 4068–4079 (2014).
<https://doi.org/10.1021/cg500699z>
- [57] Gordon T., Perlstein B., Houbara O., Felner I., Banin E., Margel S.: Synthesis and characterization of zinc/iron oxide composite nanoparticles and their antibacterial properties. *Colloids and Surfaces A: Physicochemical and Engineering Aspects*, **374**, 1–8 (2011).
<https://doi.org/10.1016/j.colsurfa.2010.10.015>
- [58] Kim S., Ghafoor K., Lee J., Feng M., Hong J., Lee D-U., Park J.: Bacterial inactivation in water, DNA strand breaking, and membrane damage induced by ultraviolet-assisted titanium dioxide photocatalysis. *Water Research*, **47**, 4403–4411 (2013).
<https://doi.org/10.1016/j.watres.2013.05.009>
- [59] Wang L. L., Hu C., Shao L. Q.: The antimicrobial activity of nanoparticles: Present situation and prospects for the future. *International Journal of Nanomedicine*, **12**, 1227–1249 (2017).
<https://doi.org/10.2147/IJN.S121956>
- [60] Morones J. R., Elechiguerra J. L., Camacho A., Holt K., Kouri J. B., Ramirez J. T., Yacaman M. J.: The bactericidal effect of silver nanoparticles. *Nanotechnology*, **16**, 2346–2353 (2005).
<https://doi.org/10.1088/0957-4484/16/10/059>
- [61] Poltue T., Karuna C., Khrueduangkham S., Sehanam S., Promoppatum P.: Design exploration of 3D-printed triply periodic minimal surface scaffolds for bone implants. *International Journal of Mechanical Sciences*, **211**, 106762 (2021).
<https://doi.org/10.1016/j.ijmecsci.2021.106762>
- [62] Ali D., Ozalp M., Blanquer S. B., Onel S.: Permeability and fluid flow-induced wall shear stress in bone scaffolds with TPMS and lattice architectures: A CFD analysis. *European Journal of Mechanics – B/Fluids*, **79**, 376–385 (2020).
<https://doi.org/10.1016/j.euromechflu.2019.09.015>
- [63] Sun C. T., Vaidya R. S.: Prediction of composite properties from a representative volume element. *Composites Science and Technology*, **56**, 171–179 (1996).
[https://doi.org/10.1016/0266-3538\(95\)00141-7](https://doi.org/10.1016/0266-3538(95)00141-7)
- [64] Santos J., Pires T., Gouveia B. P., Castro A. P., Fernandes P. R.: On the permeability of TPMS scaffolds. *Journal of the Mechanical Behavior of Biomedical Materials*, **110**, 103932 (2020).
<https://doi.org/10.1016/j.jmbbm.2020.103932>